# Growth of high quality a-(Si,Ge):H films using low pressure, remote ECR plasma technique

by

Sanjeev Kumar Kaushal

A Thesis Submitted to the

Graduate Faculty in Partial Fulfillment of the

Requirements for the Degree of

MASTER OF SCIENCE

Department: Electrical and Computer Engineering
Major: Electrical Engineering



Iowa State University
Ames, Iowa

1995

# TABLE OF CONTENTS

# ABSTRACT

We report on the growth chemistry and properties of high quality a-(Si,Ge):H films using a low pressure, remote ECR discharge. The technique consists of using intense H and He plasma beams to grow the films from a mixture of silane and germane. The growth temperatures were fairly high, in the range of 300-350°C. The films were characterized using activation energy, photo-conductivity and sub-gap absorption techniques. The hydrogen content in the films was also determined using FTIR spectroscopy technique. We find that the films grown using He plasma beams had very low Urbach energies for valence band tails, and also a correspondingly low sub-gap absorption coefficient $\alpha$. The values of both subgap $\alpha$ and Urbach energies were lower than for comparable films deposited using triode-glow discharge deposition. We also find that the use of He allows us to achieve a lower Tauc bandgap, for a given Si:Ge ratio in the solid phase than for comparable glow discharge films. Even the Tauc bandgap of a-Si:H, deposited using He-ECR discharge was much lower (1.67eV) than that of the films deposited using H-ECR discharge (1.75eV). The corresponding H concentrations were also lower in He-ECR films, and yet the electronic properties were superior compared to a material with the same Tauc gap deposited using H. This clearly indicates that ion bombardment by He ions produced by intense ECR discharge, when combined with high dilution ratio to prevent gas phase reactions, leads to improvement in the film properties such as disorder and subgap $\alpha$. Thus we have tried to show that the chemistry of growth and deposition conditions play a major role in determining the properties of a-(Si,Ge):H thin film material.

# I. INTRODUCTION

## A. Properties of a-Si:H

### 1. Continuous Random Network

Amorphous silicon is a fundamentally different material from crystalline silicon, although the silicon bonds create a similar semiconducting electronic structure. Complete reviews of the current understanding of amorphous semiconductor material properties are included in the references [1-4], and a brief overview is presented in this section. Amorphous silicon does not have a crystalline lattice, so the traditional means of describing the band diagram using Bloch waves, Brillouin zones and lattice parameters do not apply. Instead, a more basic approach using the bonds found in the amorphous structure is generally used.

Amorphous silicon is best described as a continuous random network that has short range order, but no long range order as in crystalline silicon [5]. Silicon atoms, having four valence electrons, bond covalently to four neighboring silicon atoms with the same average bond lengths and bond angles as in crystalline material. This four-fold coordination only extends for a short distance, though. Disorder in the form of variations in the bond lengths and angles destroys the symmetry after a few interatomic spacings. These variations in bond dimensions also allow atoms in the network to have a variety of correlation numbers, this randomness is what makes amorphous silicon uniquely capable as a photovoltaic device, but may also be the source of the inherent instability of the material.

Variations in bond dimensions and correlation number are shown in the schematic network model of Figure 1.1. A silicon atom that has a coordination number of three has one unpaired electron, known as a dangling bond. These dangling bond defects create an electronic

energy state that appears near the center of the semiconductor energy gap. It is this type of defect that makes pure amorphous silicon unusable for electronic devices.

When hydrogen is present during the formation of the network, it efficiently removes the dangling bond defect by bonding with the unpaired silicon valence electron. A hydrogen concentration of approximately ten atomic percent is required to reduce the dangling bond defect density to device-quality levels. A higher concentration of hydrogen reduces the material quality by promoting the formation of weak Si-H bonds and creating microvoids containing high concentrations of hydrogen. Lower concentrations on the other hand, leave too many dangling bond defects in the material.

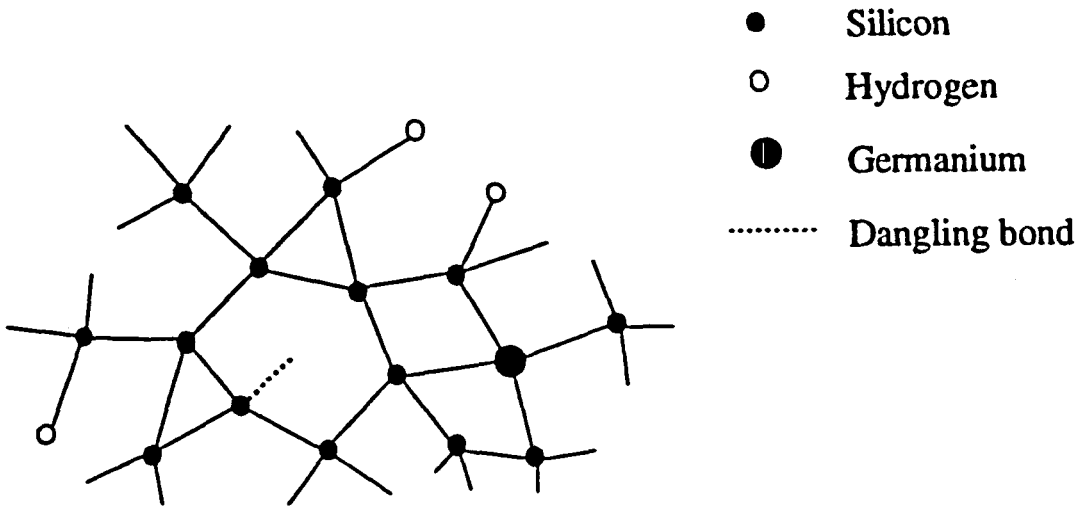


Figure 1.1. Representation of the hydrogenated amorphous silicon continuous random network and the incorporation of germanium.

Also depicted in Figure 1.1 is the effect of incorporation of a germanium atom. The network easily accommodates atoms of different bond dimensions, allowing the continuous variation in the energy gap linearly between that of pure a-Si:H and pure a-Ge:H. The same is true for incorporation of carbon in to the network. These alloys are used to enhance photon absorption and photogenerated carrier collection through the use of bandgap engineering.

Unfortunately, introducing atoms other than silicon or hydrogen degrades the quality of the material. Both the electrical and structural properties of a-(Si,Ge):H degrade with increasing germanium content, limiting the useful range of bandgaps available for devices [6]. The practical lower limit for the bandgap is about 1.4eV for solar cell devices. It has been reported that properties of pure a-Ge:H are better than the a-(Si,Ge):H alloy properties, although for different deposition conditions than those used for a-Si:H deposition [7]. This indicates that the alloyed material can be improved if the proper deposition conditions can be found, rather than the only possibility that the addition of germanium will simply result in higher defect levels.

Another aspect of the continuous random network of amorphous semiconductors is the lack of indirect or momentum assisted recombination paths. In crystalline semiconductors indirect recombination paths along a crystal axis sometimes define the energy gap since the energy for this path is lower than the direct recombination path. This is not true in a-Si:H since it has no crystal axes. As a result, a-Si:H is always a direct bandgap material. Depending upon the hydrogen content, the band energy of a-Si:H is in the 1.7eV to 1.8eV range. This value is lower than the 3.0eV for the direct bandgap of crystalline silicon and results in significantly higher absorption coefficients for photons in the visible wavelength range.

The inherent disorder of the amorphous network is also the reason for the direct bandgap energy of a-Si:H being lower than that of the crystalline silicon direct bandgap. The four valence electrons of an unbound silicon atom occupy two 3s and and two 3p electronic orbitals or energy states. When the silicon-silicon bands form during deposition, the electron interaction splits these energy states into bands. The highest energy band becomes the

conduction band. When the bond energies vary due to differences in bond length or angle as in the amorphous network, the electron interactions create a wider range of allowed electronic states, and the energy bands become broader. As a result, the top of the valence band moves up in energy and the bottom of the conduction band moves down in energy as compared to the crystalline energy bands. Then, the resulting bandgap for the amorphous silicon network has a lower energy value than in the crystalline counterpart.

The presence of hydrogen in the network also affects the electronic structure. The incorporation of hydrogen reduces the band broadening by passivating dangling bonds and removing some of the weak silicon bonds, so the a-Si:H bandgap is increased somewhat by increasing the hydrogen content. Varying the hydrogen content only provides about a tenth of an electron-volt of useful change in the bandgap, though since straying too far from the optimum hydrogen content increases the defect density, as explained earlier.

## 2. Electronic Structure and Transport

In general, the energy band diagram of amorphous semiconductor is created by the electron orbital interactions between the various types of bonds in the network. A continuous distribution of allowed energy states is created because of the disorder in the network. Thus, in amorphous semiconductors, the notion of a forbidden energy gap, as used for the crystalline counterpart is not valid, since there is no forbidden region without allowed energy states. Several different definitions are used to designate a bandgap energy, and some of these are described next.

One method of designating a bandgap is to use the carrier transport properties. The states for which energy 'E' approaches the critical energies for valence and conduction band ($E_V$, $E_C$) are called extended states. The conduction of electrons and holes in these extended states of the conduction and valence bands is obstructed by the frequent trapping in localized

states near the band edges. This method of conduction is known as dispersive transport and is represented by the Figure 1.2 [8-9]. The localized state density dominates the extended state density in the regions leading up to the conduction and valence band edges. Therefore, the demarcation between extended states and localized states at each energy band defines the gap known as the mobility gap or the pseudogap.

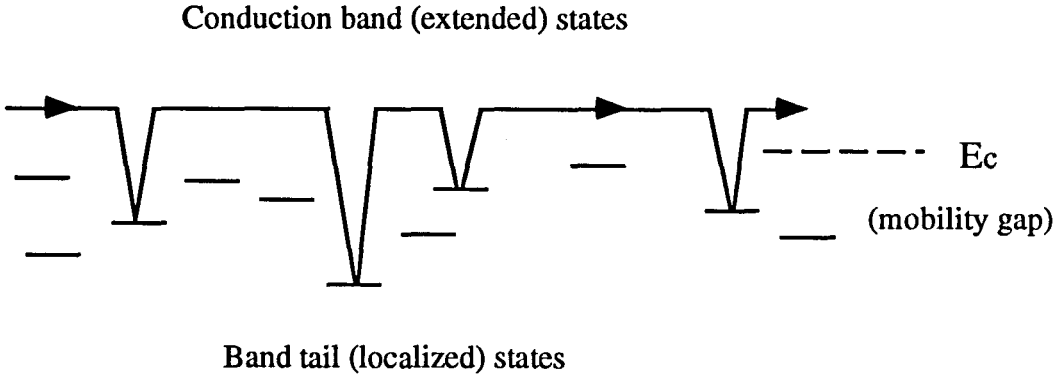


Figure 1.2. Dispersive transport of an electron in the conduction band.

The localized states below the conduction band and above the valence band are known as band tails and have an exponential energy distribution. A commonly used band model of a-Si:H is shown in Figure 1.3. Because the localized states and extended states cannot coexist at a given energy, there are sharp divisions between them that form the valence and conduction band edges, $E_V$ and $E_C$. The allowed conduction mechanism in low mobility localized states is thermally activated hopping in tail states. Hopping is defined as tunneling of electrons from localized states in to adjacent localized states. The energy difference between these states is compensated by the emmision or absorption of phonons. The fermi level position $E_f$,for undoped a-Si:H is usually slightly closer to $E_C$ than $E_V$.

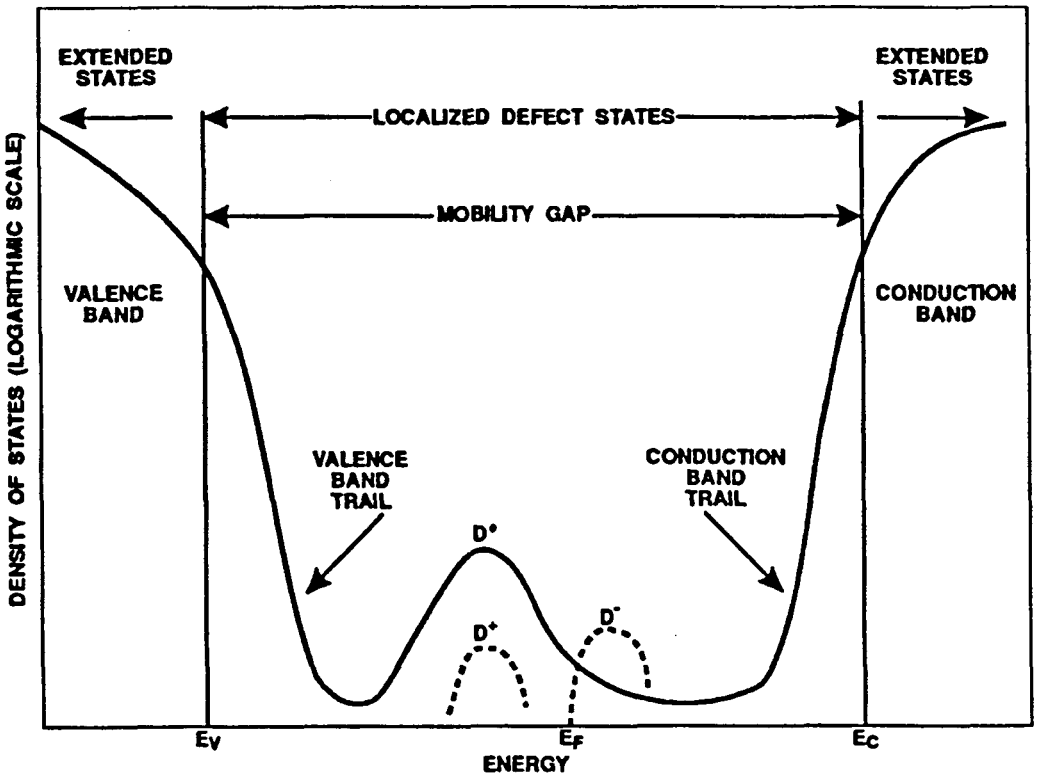


Figure 1.3. Electronic density of states in the mobility gap of a-Si:H.

The densities of extended states and band tail states also determine the absorption of photons. This provides yet another way of defining the bandgap. The absorption coefficient depends upon the extended states density distribution, which may be approximated as parabolic near the band edges. Under this approximation the absorption coefficient '$\alpha$' follows the relation

$$\sqrt{\alpha h\nu} = B\left[h\nu - E_g\right] \qquad (1.1)$$

where hν is the energy of the incident photon, 'B' is material dependent prefactor, and $E_g$ is the bandgap. The prefactor B for amorphous semiconductors is given by

$$B = \sqrt{\frac{4\pi\sigma_o}{ncE_w}} \tag{1.2}$$

where $E_w$ is the extent of band tailing.

The bandgap measured above is known as the Tauc gap because Tauc et. al. made this approximation. Since the bands may not be parabolic at the edges [10], the above gap is not entirely accurate.

One other method of defining an energy gap is to simply designate the energy where photon absorption reaches a value of $10^4$ $cm^{-1}$ and is known as the $E_{04}$ gap.

The optical absorption has an exponential energy dependence in the vicinity of the band gap energy given as

$$\alpha h\nu = \alpha_o \exp\left[\frac{E - h\nu}{E_o}\right] \tag{1.3}$$

where hν is the photon energy.

The energy $E_o$ is known as Urbach energy because the exponential absorption edges were first observed by Urbach in the absorption spectrum of AgBr and the exponential tail is called the Urbach edge. The valence band tail characteristic energy of a-Si:H is usually determined by d(hν)/d(lnα) from the straight line region of the sub-bandgap optical absorption coefficient α (in logarithmic scale) vs. photon energy (hν) plot. An important consequence of the tail states is that nonradiative recombination can occur, which limits the lifetime and is thus inescapable for amorphous semiconductors. This is important for photovoltaic applications,

since a limitation of the lifetime also limits the open-circuit voltage in solar cells. The valence band tail of low defect density a-SiH has an exponential slope of about 45 meV and is broader than the conduction band tail for which it is usually smaller than 35 meV [11]. Thus it dominates the joint density of states. Since the slope, $E_o$, of the Urbach absorption reflects the shape of the valence band tails, it follows that $E_o$ varies with structural disorder. For example, one measure of the disorder is the average bond angle variation, which is measured from the width of the vibrational spectrum using Raman spectroscopy. The defect density is another measure of disorder and also increases with the band tail slope. Therefore $E_o$ is very good measure of material quality. The smaller the value of $E_O$, the better the film quality. Thus by establishing the correlation between $E_o$ and other material parameters such as the alloy content, transport parameters and optical characteristics would provide us with a useful technique for estimating alloyed material quality. Finding this correlation will be one of the goals of the project.

The deep level density of the states shown in Figure 1.3 is created by point defects in the material such as dangling bonds. These mid-gap defect states can also serve as recombination centers that degrade the electronic properties of the semiconductor. The dangling bonds in a-Si:H can be positively charged ($D^+$) when unoccupied ($sp^2$), neutral ($D^0$) when singly occupied ($sp^3$), and negatively charged ($D^-$) when doubly occupied ($s^2p^3$). Neutral dangling bonds can be measured by electron spin resonance (ESR). In hydrogenated material, these deep defects have a low density and the Fermi level can move easily within this region. The Fermi energy of intrinsic material is located near the minimum in defect density which is slightly closer to the conduction band than the valence band. The exact distribution and source of these deep level energy states is still the subject of ongoing debate. One of the simplest ways to model this region is by assuming it to be an exponential distribution. More sophisticated distributions such as the mid-level gausian distributions of the defect pool model are also currently used to explain all of the experimental results.

## B. Characteristics of Hydrogenated Amorphous Si,Ge

Hydrogenated amorphous silicon alloys are so far, the only type of low-bandgap materials used in multiple junction amorphous silicon solar cells. Although a-SiGe:H is currently the best low gap material, it has much poorer electrical and photoelectric properties than a-Si:H. The photoelectronic properties deteriorate with increasing Germanium content and the deterioration proceeds rapidly as the Ge content of the alloy exceeds 40%. Some of the best reported characteristics for glow discharge deposited a-(Si,Ge):H materials with bandgap ($E_g$), values of 1.5eV are $\sigma_l$ = 3.0 E-04 S/cm [12], $n\mu t$ = 1.0E-06 $cm^2$/volt [13], $\sigma_d$ = 1.4E-10 S/cm [14], $\sigma_l/\sigma_d$ = 1.8E+04 [15], Urbach parameter = 46 meV, ESR spin density = 6.5E+15 $cm^{-3}$, and density of states at the Fermi level obtained by measuring the space charge limited currents using $n^+$- i - $n^+$ structures = 2E+16 $V^{-1}cm^{-3}$.

The basic material parameters of a-(Si,Ge):H alloys in general can be summarized in the following way:

| | |
|---|---|
| Optical(Tauc) gap ($x_{Ge}$) (eV) [16] | $E_{opt} = 1.7 - 0.7\ x_{Ge}$ |
| Electronic affinity ($x_{Ge}$) (eV) [17] | $X = 3.7 + 0.5\ x_{Ge}$ |
| Mobility gap (eV) | $E_\mu = E_{opt} + 0.18eV$ |
| Electron band mobility ($cm^2V^{-1}s^{-1}$) [18] | $10 < \mu_{n,o} < 20$ |
| Hole band mobility ($cm^2V^{-1}s^{-1}$) [18] | $1 < \mu_{p,o} < 10$ |
| Electron drift mobility ($cm^2V^{-1}s^{-1}$) [19] | Strong function of $E_{opt}$ |
| Hole drift mobility ($cm^2V^{-1}s^{-1}$) [19] | Strong function of $E_{opt}$ |
| Conduction band DOS ($cm^{-3}$) [20] | $N_C$ = 3.0 E+19 |
| Valence band DOS ($cm^{-3}$) [20] | $N_V$ = 3.0 E+19 |

| | |
|---|---|
| Tail states characteristic energy [21] | |
| conduction band(eV) | $E_A = 0.030 - 0.050$ |
| valence band(eV) | $E_D = 0.050 - 0.060$ |
| Tail states density prefactor | |
| conduction band ($cm^{-3}\ eV^{-1}$) | $G_{Ao} = 1.0E+21$ |
| valence band ($cm^{-3}\ eV^{-1}$) | $G_{Do} = 1.0E+21$ |
| Acceptor-like Gaussian defect state [22] | |
| above valence band (eV) | $E_{ac} = 0.81+0.24\ E_{opt}$ |
| | $(1.5 < E_{opt} < 1.8eV)$ |
| | $E_{ac} = 0.11+0.64\ E_{opt}$ |
| | $(1.16 < E_{opt} < 1.5eV)$ |
| FWHM (eV) | $W_{ag} = 0.4$ |
| Donor-like Gaussian defect state [22] | |
| below conduction band (eV) | $E_{do} = 0.19 + 0.38\ E_{opt}$ |
| FWHM (eV) | $W_{dg} = 0.4$ |
| Capture cross section ($cm^2$) [23] | |
| neutral band tail states | $10^{-17}$ |
| charged band tail states | $10^{-15}$ |
| neutral midgap states | $10^{-15}$ |
| charged midgap states | $10^{-14}$ |

Improvement of a-SiGe:H prepared from gas mixtures of silane, germane, and hydrogen by RF glow discharge has been attempted using an ultra high vacuum (UHV) (10.0E-09 Torr base vacuum) deposition system. Impurities in the resulting films were

reduced: oxygen from 4.0E+19 to 1.0E+19, nitrogen from 8.0E+18 to 4.0E+17, and carbon from 4.0E+19 to 2.0E+18 $cm^{-3}$ as compared to films deposited by the same researchers in a conventional glow discharge system. The photoluminescence was more than five times higher than that for conventional glow discharge films, suggesting that no radiative recombinations and possibly, the tail state density in the films were reduced by reduction in impurities. The refractive indices were higher than that of the conventional glow discharge films over the bandgap range of 1.4 to -1.55 eV (Eg. 3.7 vs. 3.72 at 1.5eV), indicating higher structural density. Other parameter comparisons between the 1.52eV Eg, UHV deposited films and conventional films were:

$\sigma_l$ = 2.7E-04 vs 1.6E-04 S/cm, $E_u$ = 46 vs 49 meV, ESR spin density = 6.5E+15 vs 1.1E+16 $cm^{-3}$.

The question now arises whether anything can be done to avoid the deterioration of photoelectronic properties with increasing germanium content. The following section describes some of the attempts that researchers have made to accomplish this and their results.

The optical bandgap is directly related to Ge content of the alloy; as the Ge content, x, of a-$Si_{1-x}Ge_x$:H increases from 0 to 100% ($0<x<1$), the optical bandgap decreases monotonically from about 1.75eV to 1.1eV (see Figure 1.4).

The bandgap in eV is mathematically described as roughly 1.76 - 0.78x. The deposition parameters for the data in Figure 1.4 are listed in Table 1.1.

Bandgap also depends upon certain deposition conditions such as temperature. The substrate temperature during deposition in turn effects the hydrogen content in the film; increased temperature results in lower hydrogen content and lower bandgap. However, the H and Ge contents of a-SiGe:H films are not independent parameters. Fortmann and Tu [1988] showed the interrelation between Ge content, temperature, hydrogen content and optical bandgap.

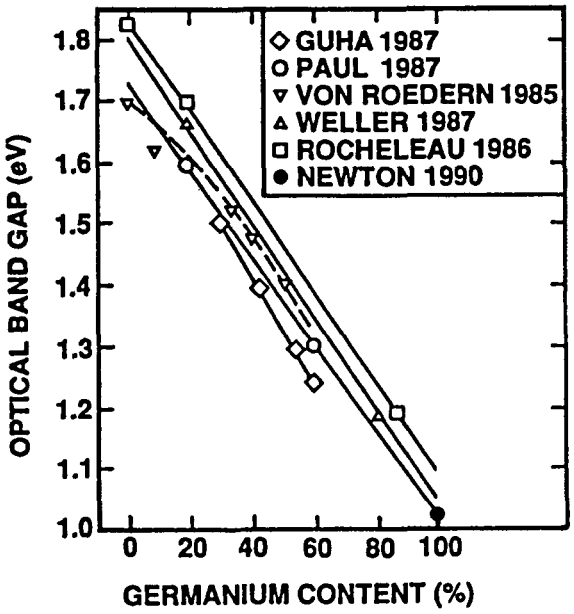


Figure 1.4. The effect of germanium content on the optical bandgap of a-SiGe:H for various deposition methods and conditions shown in Table 1.1 [24].

The differences in bandgap that various researchers have observed for a given amount of Ge are attributable to variations in hydrogen content and in the determination of the optical bandgap (normally established from Tauc plots), rather than the deposition method or feed-gas.

The Urbach parameter, $E_u$, increases for films deposited by glow discharge from about 43 meV for a-Si:H to 56 meV for a-SiGe:H with a 40% Ge cotent (see Figure 1.5). Different Urbach energy measurements cannot be directly compared unless the film thickness is reported.

Table 1.1. Deposition parameters for data in Figure 1.4 [24].

| Method | Electrode Conf. | Feed gas | Dilutent | Temperature (°C) | Reference |
|---|---|---|---|---|---|
| RFGD | Diode | $Si_2H_6/GeH_4$ | $H_2$ | 225 | Guha 1987 [25] |
| RFGD | Diode | $SiF_4/GeF_4$ | $H_2$ | 300 | Paul 1987 [26] |
| RFGD | Diode | $SiH_4/GeH_4$ | None | 320 | v.Roedem 1985 [27] |
| DCGD | Triode | $SiH_4/GeH_4$ | $H_2$ | NA | Weller 1987 [28] |
| Photo | ----- | $Si_2H_6/GeH_4$ | $H_2$ / He | 240 | Rocheleaue 1987 |
| DCGD | Diode | $GeH_4$ | $H_2$ / Ar | 240 / 340 | Newton 1990 [30] |

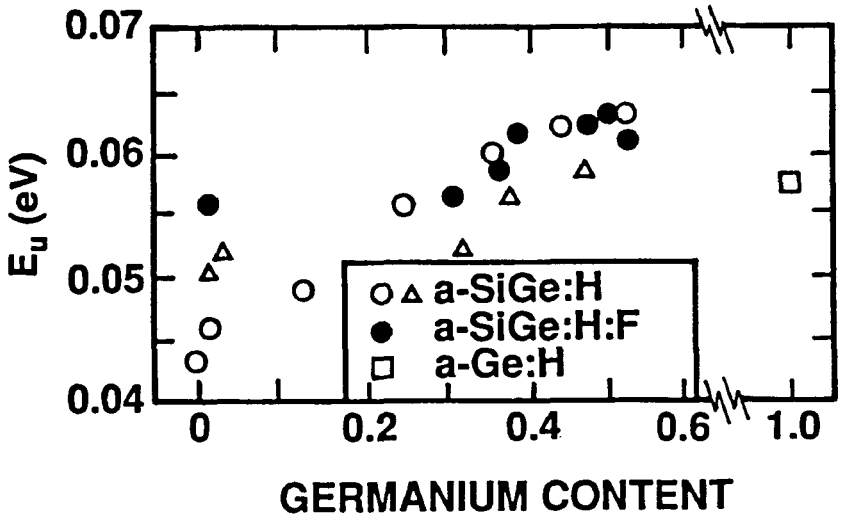


Figure 1.5. Effect of Germanium content on the Urbach parameter $E_u$ for a-SiGe:H [24].

[Mackenzie et al. 1985,von Roedern et al. 1985,Newton and Kritikson 1990]

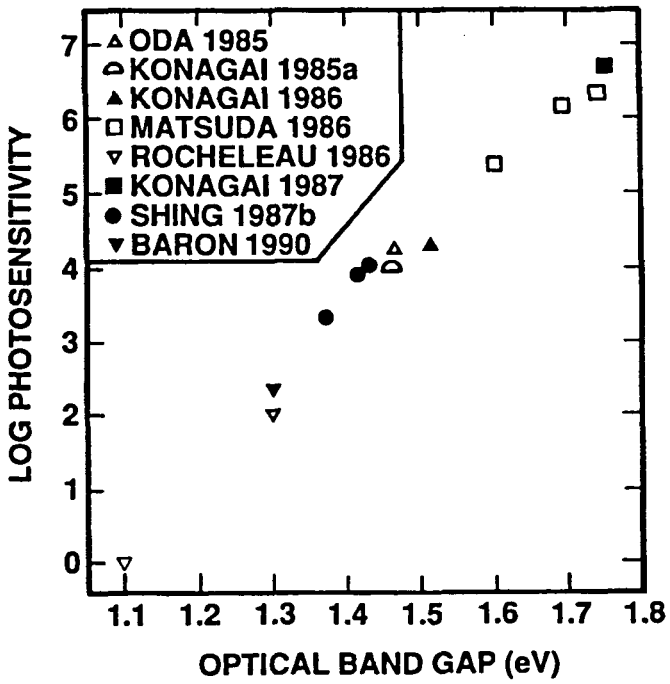


Figure 1.6. The effect of the optical bandgap on the best photosensitivities recorded for a-SiGe:H films produced by glow discharge and photo-CVD [24].

Most researchers have found that photoconductivity decreases and dark conductivity increases as bandgap decreases(with increasing Ge content), resulting in decreases in the photosensitivity with decreasing bandgap (see Figure 1.6).

Photosensitivity is the ratio of AM1.5 $\sigma_l$ to $\sigma_d$. The logarithm of photosensitivity decreases linearly from 7.0E+6 at 1.75eV to 1.0E+03 at 1.35eV. Examples of the change in AM1.5 $\sigma_l$ with bandgap are from 2.0E-04 S/cm for a-Si:H to 2.0E-05 S/cm for 1.5eV a-(Si,Ge):H; the corresponding change in $\sigma_d$ is from 5.0E-11 S/cm to 2.0E-09 S/cm. However,

Dalal et.al and Konagai et.al showed an essentially constant $\sigma_d$ vs $E_g$ for a-(Si,Ge):H films produced by glow discharge and photochemical vapor deposition. The photoconductivity of a-(Si,Ge):H is also a strong function of the hydrogen content. Fortman showed a decrease of $\sigma_l$ from 1.1E-06 S/cm at 3 atomic % H to 3.0E-07 S/cm at 9 atomic % H for a film with 60 atomic % Ge.

In the best films produced by glow discharge, the $n\mu\tau$ product for electron decreases from about 1.0E-05 $cm^2/V$ for a-Si:H to 1.0E-06 $cm^2/V$ for a-(Si,Ge):H with 40% Ge content. The $\mu\tau$ product of holes is about 1/3 that for electrons. Films deposited at higher temperatures (e.g.270°C instead of 200°C) have superior electron transport and show a relatively small change in $\mu\tau$ in the bandgap range of 1.3 to 1.5eV compared to that in the 1.5-1.65eV.

For a-(Si,Ge):H, the diffusion length is about 50nm for material having the bandgap in the range of 1.1-1.5eV. The diffusion length is correlated to Urbach energy : the log(diffusion length) decreases linearly with increasing Urbach energy from 0.1 micrometer at 50meV to 0.05 micrometer at about 70meV, and then remains constant.

It was found my Mitchell et. al [1985] that hydrogen content reduces with increase in Ge content in the alloy. One of the reasons for this is that hydrogen attaches preferentially to Silicon rather than to Germanium. As a result of this preferential attachment of hydrogen to silicon and the weakness of the Ge-H bonds, relatively more defects in a-SiGe:H alloys are Ge dangling bonds than Si dangling bonds. Stutzmam et.al observed that, when the Ge content in a-SiGe:H is more than 50%, the Ge dangling bond density in high quality films deposited by RF glow discharge decomposition of $SiH_4$ and $GeH_4$ is more than 5.0E+17 $cm^{-3}$ whereas the Si dangling bond density in the same films is less than 1.0E+15 $cm^{-3}$.

## C. Growth Chemistry

Growth chemistry [31] plays a major role in the deposition of high quality material using plasma deposition. In a plasma, several chemical reactions can take place and many species can be generated. As an example, silane can be fractionated into $SiH_3$, $SiH_2$ and SiH radicals, and it is also possible for these radicals to interact with each other, and with the parent molecule. Moreover, if the concentrations of the different species of radicals are comparable, then the growth of the film can become complicated. As an example, if both $SiH_3$ and $SiH_2$ are present, then insertion reaction leading to growth can be shown in Figure 1.7. As it is obvious from Figure 1.7, after an insertion reaction, the surface of the material becomes non-homogeneous, with some sites being empty, ready to accept another radical, but other sites are passivated with H, and this H has to be removed before another radical can insert itself. Thus, multi-species reactions can lead to non-homogeneous growth which will lead excessive hills, valleys and voids. At the low growth temperatures, the structure cannot homogenize by diffusion of radicals, and these defects will be frozen in, therefore it is necessary to achieve a growth chemistry where one can lead to predictable growth from one species.

For growth of a-(Si,Ge): H, these conditions become even worse. The two primary precursors, silane and germane fractionate at very different rates because of the difference in bond strengths of Si-H (3.3 eV) and Ge-H (3.0 eV) . The Ge-H bonds lie sufficiently high enough in the density of states, such that they intersect the chemical potential of H and therefore should result in many Ge dangling-bond defects, but few Si dangling bonds. Experiments confirm these predictions. Improved a-(Si,Ge):H material should result from raising the H chemical potential above the Ge-H bonds, for example, by hydrogen dilution of the plasma. Therefore, it is essential that the chemical reaction proceed in a predictable way, or that extra energy be imparted to the surface to improve the diffusion of radicals, and hence the properties of the material.

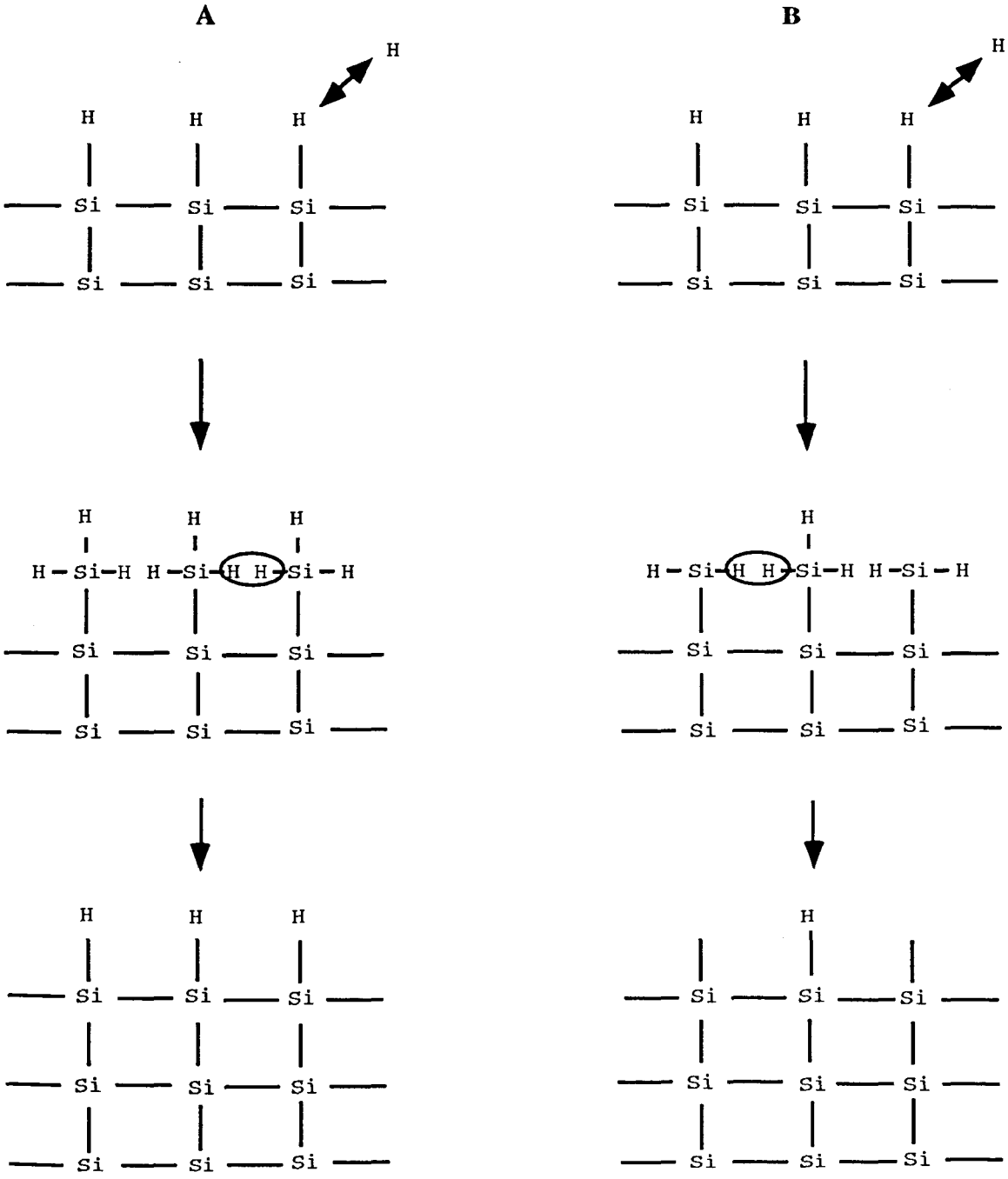


Figure 1.7. Steps in the growth of a-Si films due to the insertion of $SiH_3$ (A) and $SiH_2$ (B) radicals.

One predictable way of forcing the reaction is to use an excess of hydrogen. With the high concentrations of 'H' present in the plasma, the predictable chemical reactions would be

$$H + SiH_4 = H_2 + SiH_3 \quad (1.4)$$

$$H + GeH_4 = H_2 + GeH_3 \quad (1.5)$$

Thus excess of H will force the production of silyl ($SiH_3$) and germyl ($GeH_3$) radicals, and we will get a somewhat homogeneous insertion reaction.

We still have a problem with the different mobilities of germyl and silyl radicals on the surface. To overcome this problem, it is useful to use ion bombardment, either with H or with an inert gas such as He. Therefore, it is not surprising that the use of highly diluted H plasmas, with high ion-bombardment energies, has led to the growth of better a-(Si,Ge):H films. Another advantage of H dilution is that the presence of excess H prevents the reactions between the radicals, thereby preventing the formation of higher polymers, which will produce highly nonuniform films.

Another aspect of the growth chemistry deals with the relationship between bandgap and Ge content. The band-gap of a-(Si, Ge):H alloy depends not only on the Ge content; but also on what happens during growth. Appropriate H etching can reduce the void structure but, excess H etching during growth can lead to a widening of the gap, thereby requiring more Ge to achieve the given bandgap. In general, more Ge incorporation will lead to greater non-homogeneities in the film and thus poorer film properties. To overcome this, it may be useful to limit the amount of H-induced etching during growth. A technique such as neutral ion bombardment may allow both increased surface mobility and reduced etching, thereby leading to a lower gap and yet a better material for a given Ge concentration.

## D. Scope of Research

Hydrogenated amorphous silicon germanium alloys (a-$Si_{1-x}Ge_x$:H or simply a-SiGe:H) are so far the only type of low-bandgap materials used in multiple-junction amorphous silicon solar cells. The reason for the interest in multi-junction devices is their potentially higher conversion efficiencies than single junction devices. Although a-SiGe:H is currently the best low-bandgap material, it has much poorer electrical and photoelectric properties than a-Si:H (for example, reduced photoconductivity and photoluminescence and increased defect density). The photoelectronic properties deteriorate with increasing Ge content and the deterioration proceeds rapidly as the Ge content of the alloy exceeds 40% (corresponding to a bandgap of approximately 1.5eV).

The growth of high-quality a-SiGe:H films presents the experimentalist with several difficulties. Some of these are described in the following section:

1. The bond energy of germane is much lower than the bond energy of silane. As a result, during a plasma-growth process, the decomposition rate of germane is much higher than that of silane. Consequently, the Ge/Si ratio in the solid phase (in the film) is much higher than in the gas phase. The high decomposition rate of germane, in principle can also lead to severe problems related to gas-phase homogenization, i.e., reactions between decomposition products of germane produce higher order germanes, e.g., $Ge_2H_6$. These radicals can be decomposed to form $GeH_2$ and other polymers, which can lead to problems with film growth. It is generally accepted that the best a-Si:H films result when growth is from silyl ($SiH_3$) radicals, because these radicals offer a simple, step-by-step method for the growth of tetrahedrally coordinated films. It is logical to assume that a similar conclusion may be applicable to the growth of a-SiGe:H films, namely that the best film may be grown from silyl and germyl radicals, and not

from higher order polymers or from secondary products such as $GeH_2$. Therefore, the high fractionation of germane by the plasma is a cause for concern. To reduce the reactions between the various germane decomposition products, one can use several strategies. Among these are: (a) Use of low pressures, so as to avoid gas phase collisions between radicals produced by germane, and, (b) use of high dilution rate with He or H, so as to avoid collisions between germane radicals.

We decided to use a combination of both these strategies, so as to promote the growth of reproducible films of this material, while staying with germane and silane as the primary feedstocks. The reasons for choosing silane and germane as the primary gases was that these gases are readily available in ultra-high purity.

2. The very different bond strengths between Ge and H and Si and H mean that, unless one is careful, one may end up with dihydride-type bonding in the material, especially if the growth is done at low temperatures (200°C - 250°C). In order to preserve the Ge-H bond, one may inadvertently use growth conditions that lead to $SiH_2$-type bonding. This is particularly true if one goes over into the physical vapor deposition type growth, as opposed to chemical vapor deposition type mode. This is likely to be the case when the growth rate is too high. It is, therefore, not surprising that the literature shows a tremendous scatter in the properties of these films.

The work presented here focuses on the growth chemistry and properties of high quality a-SiGe:H films using a low pressure remote ECR discharge.

# II. SAMPLE PREPARATION

All samples reported in this study were deposited by using a ECR plasma deposition system. In the next few sections we shall discuss the underlying principle behind the working of this system, physical design of the system and the PECVD processing resulting in the growth of a-SiGe:H thin fims and devices.

## A. Deposition System

### 1. Fundamentals of ECR Process

The first step in the design of an ECR plasma deposition system is an understanding of the plasma source. There are several different possible arrangements for ECR sources. Variations occur in system size and shape, method of microwave introduction, and the number, position, and type of the magnets. The most commonly used arrangement is the Hitachi/NTT type ECR source shown in Figure 2.1. The plasma source is a stainless steel tube with two coils around it which are used to generate a uniform DC magnetic field. Microwaves are introduced through a quartz window on one end of the tube. The plasma is extracted from the other end of the tube.

In order to understand the plasma generation process, it is best to start with an overly simplified model. Free electrons in the plasma generation region spiral around the static magnetic field lines due to the Lorentz force. In Appendix A, it is shown that the frequency of the rotation (gyrotron frequency) is given by

$$\omega_o = \frac{qB_z}{m_e} \qquad (2.1)$$

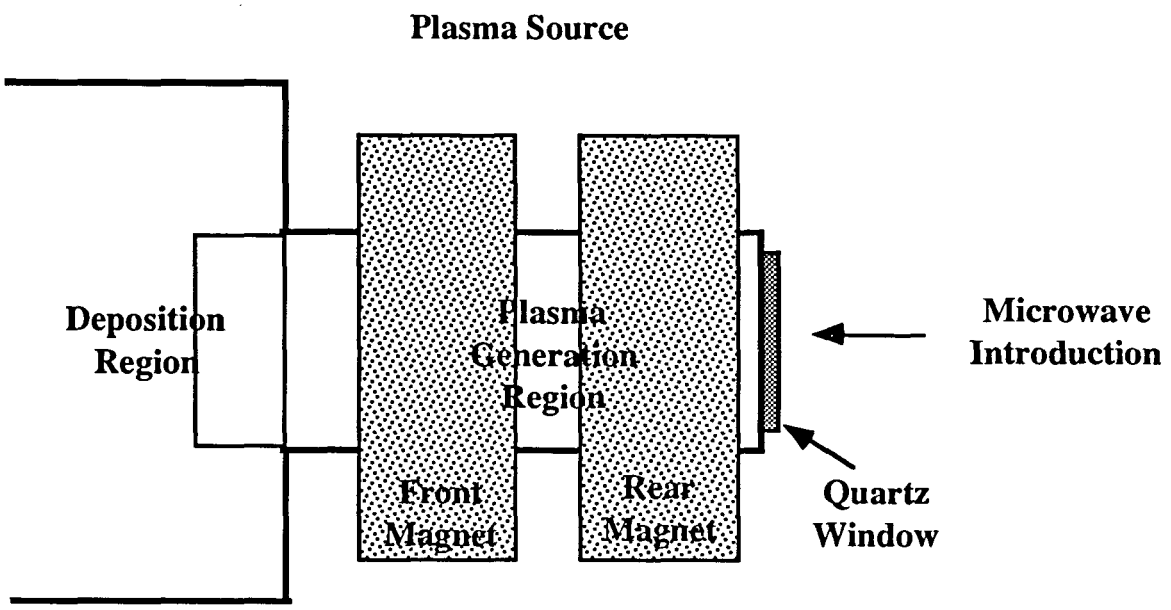


Figure 2.1. Typical arrangement for a Hitachi/NTT type ECR source.

and the radius of the spiral is given by

$$R = \left(\frac{m_e}{qB_z}\right)\sqrt{v_x^2 + v_y^2}\,. \tag{2.2}$$

Linearly polarized microwaves enter the region propagating along the axis of the static magnetic field. Linearly polarized plane waves may be equivalently expressed as two circularly polarized waves rotating in opposite directions. For example, the electric field of the linearly polarized microwaves, which can be expressed as

$$\mathbf{E} = E_0 \cos(\omega t)\mathbf{a}_y, \tag{2.3}$$

may also be written as

$$\mathbf{E} = \mathrm{Re}\left[\frac{E_o}{2}\left(a_y + ja_x\right)e^{j\omega t} + \frac{E_o}{2}\left(a_y - ja_x\right)e^{j\omega t}\right] \qquad (2.4)$$

where the first component in the bracket is a wave with right-hand circular polarization (RCP) and the second term is a wave with left-hand circular polarization (LCP).

When the gyrotron frequency and the frequency of the microwaves are the same, the electrons and the electric field vector of the RCP waves are rotating in phase with each other. This is the electron cyclotron resonance condition. The energy of the RCP microwaves goes into accelerating the electrons. The electrons then collide with neutral gas molecules, causing ionization and the formation of free radicals. Since the electrons and the LCP electric field vector are rotating in opposite directions, electron cyclotron resonance can not be the method of microwave power absorption for the LCP waves. Other possible energy loss mechanisms must be looked into for the LCP microwaves. There are many rather complex theories regarding the absorption of the LCP waves. The important result that comes out of the theories is that when the plasma density gets large enough, the LCP waves are almost completely absorbed. The point where this occurs is called the critical density, $N_{cr}$. When the density of the plasma exceeds $N_{cr}$, the microwaves are no longer able to propagate through the plasma (the amplitude decreases exponentially). By solving Maxwell's equations, the critical density is determined to be

$$N_{cr} = \frac{\omega^2 \varepsilon_o m_e}{q^2} \qquad (2.5)$$

which results in a critical density of $7.5 \times 10^{10}$ cm$^{-3}$ for the 2.45 GHz used in this work.

2. Description of ECR Reactor

The reactor used in this study is shown schematically in Figure 2.2. It consists of a microwave source operating at 2.45 GHz, which feeds power through a 3-stub tuner into a cavity. The microwave power is coupled into the cavity through a quartz window. The axial magnetic field to create the ECR condition is produced using two coils, whose relative position and magnetic field strengths are controllabe by the operator. The magnetic field needed for ECR resonance is determined by the following relationship

$$\omega_o = \frac{qB_z}{m_e} \qquad (2.6)$$

It is about 875 Gauss for 2.45 GHz microwaves. Two DC power supplies (10V, 200A)are used to power the magnets. A typical profile of the magnetic field strength is shown in Figure 2.5 later in this section. Thus, the position of the resonance plane can be changed by us and generally, we set it so that resonance plane is about 20-30 cm away from the substrate.

The plasma gases hydrogen and helium are introduced into the microwave cavity near the source end. Silane or germane (process gases) are introduced near the substrate through a separate manifold. The typical pressures, as used for growth are in the range of 10-15 mT. At these pressures, the excited H radicals have a long mean free path and they arrive at the substrate with significant energies. A simple optical emission spectroscopy (OES) system detects the presence of these radicals by looking at emission coming from a region near the substrate. The typical OES spectrum of a hydrogen plasma is shown in Figure 2.3. The peaks at 656 nm and 610 nm are noteworthy, and they represent $H_\alpha$ and $H_2$ emission lines respectively. The intensities and relative ratios of these lines change as we change the plasma conditions,thereby providing us with some information about the nature of the chemical species arriving at the substrate as we change the plasma conditions.

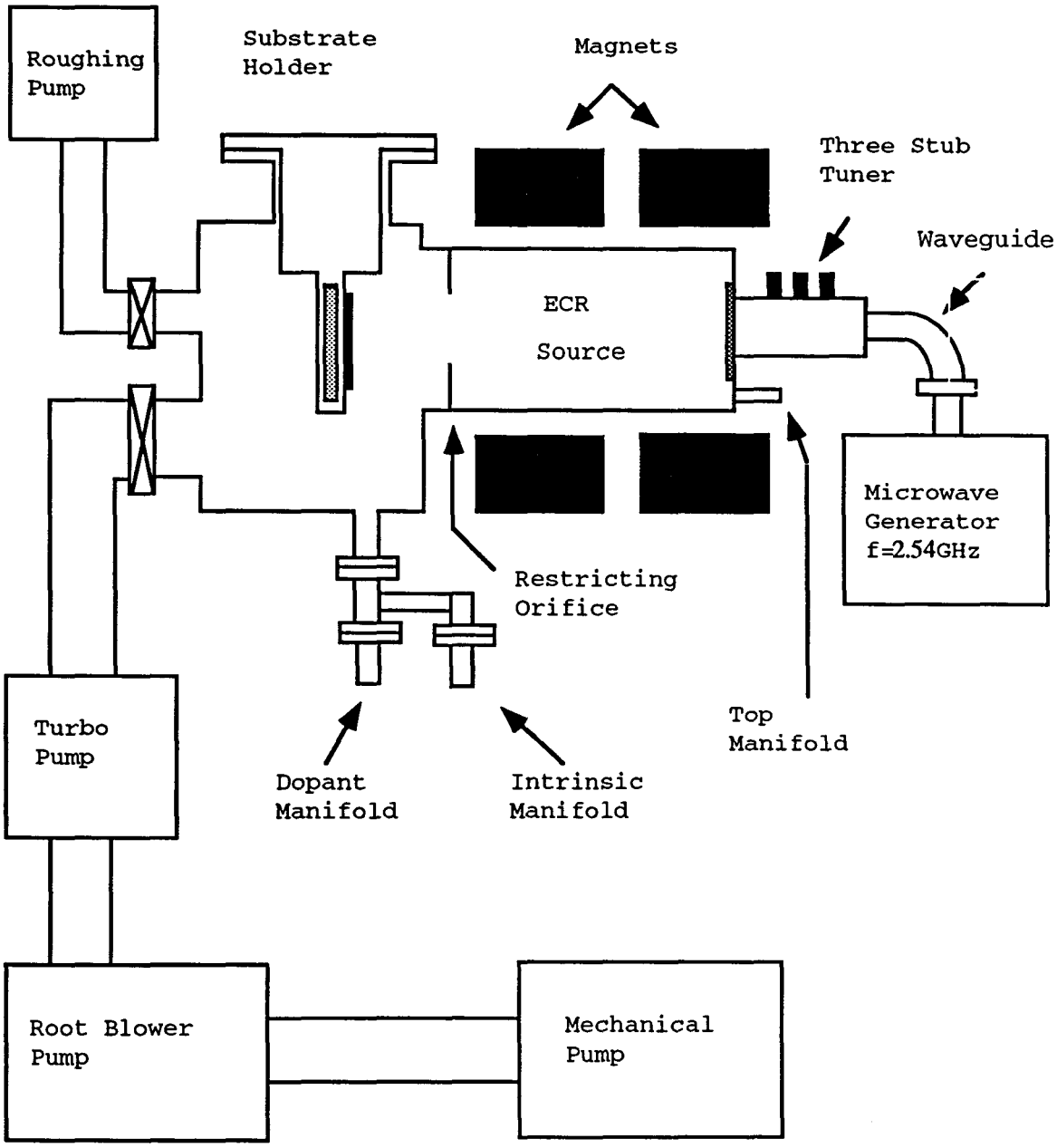


Figure 2.2. Diagram of the ECR-CVD system.

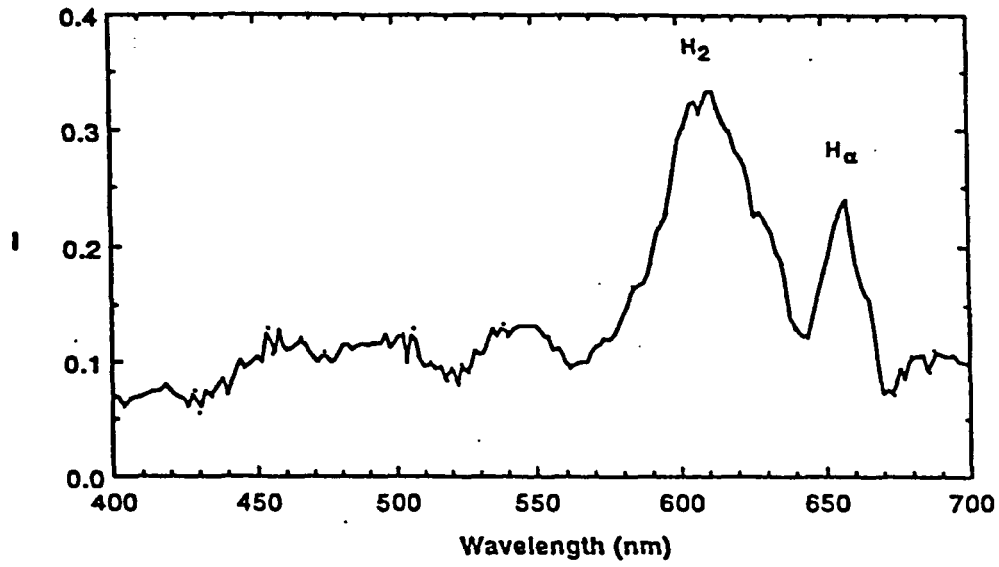


Figure 2.3. OES spectrum of ECR plasma.

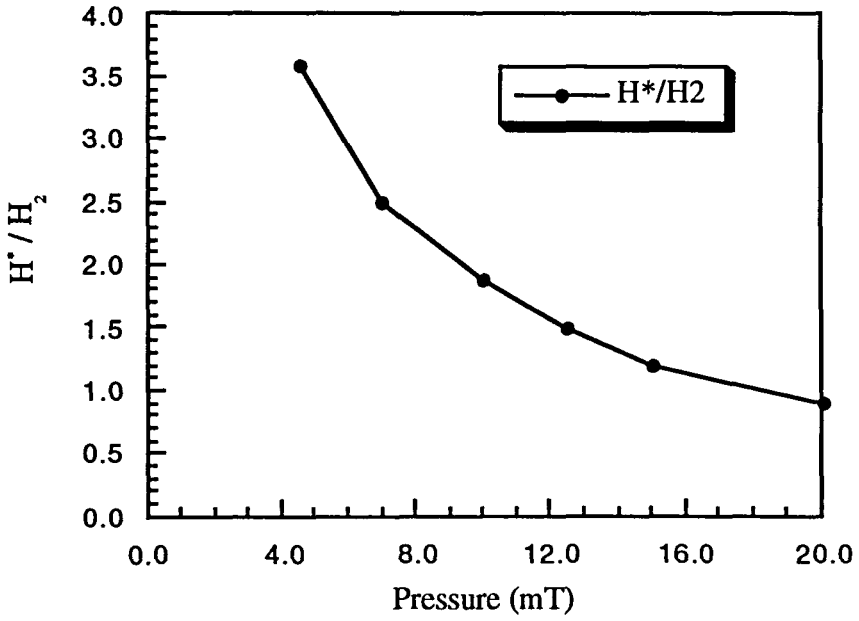


Figure 2.4. Influence of pressure on $H^*/H_2$.

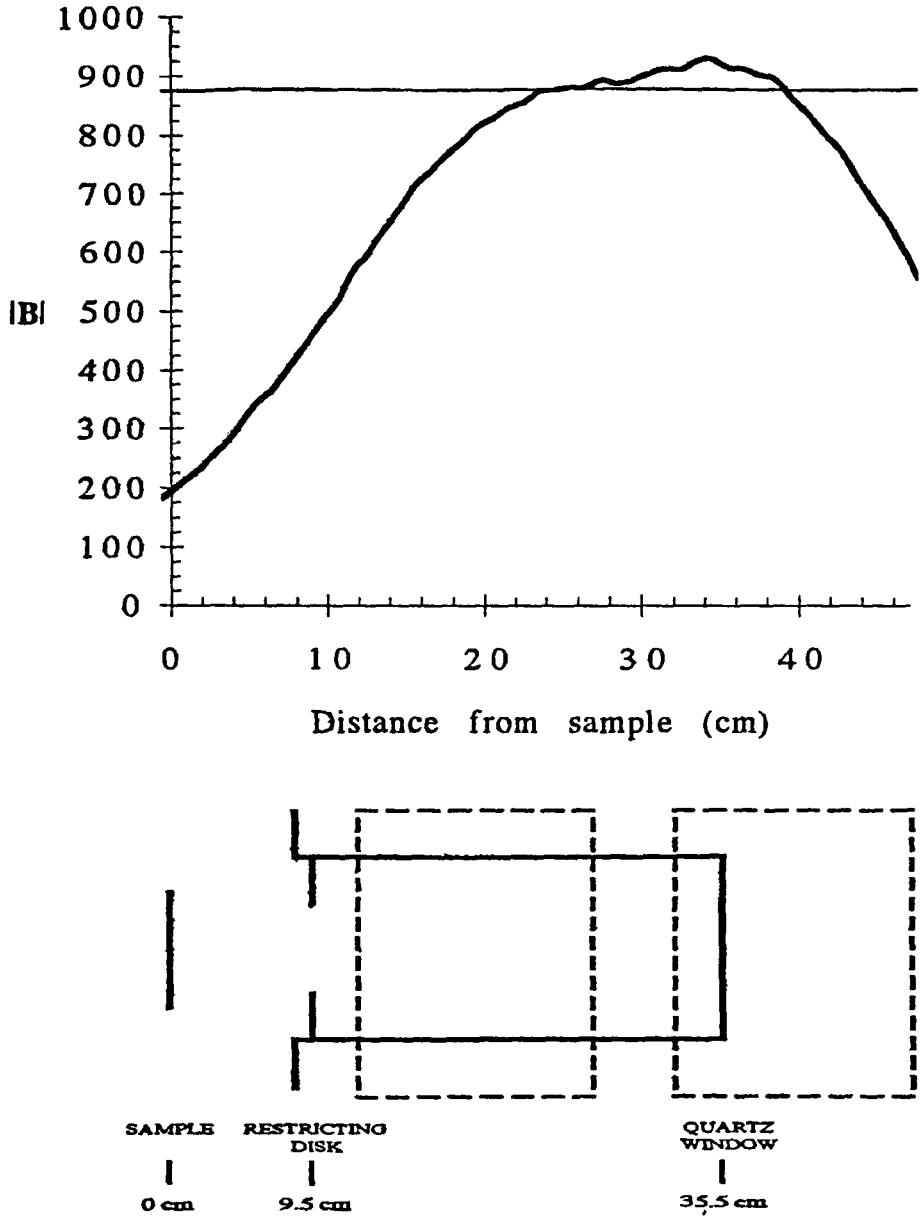


Figure 2.5. Magnetic profile present in the system during growth. This profile is made for $I_{source}$ =183 Amps and $I_{chamber}$ = 178 Amps.

In Figure 2.4 we show, what happens to the ratio of 656 nm to 610 nm lines as we decrease the pressure. Quite clearly, at lower pressures, the realative intensity of the Ha line increases, implying that more H atoms and, particularly more energetic H atoms, are arriving at these pressures.

We call our process a remote reactive plasma beam deposition process. The term remote is used to emphasize the fact that the main plasmais remote from the substrate, and that the radicals such as H and excited molecules and ions such as $He^*$, generated by the ECR plasma are playing a role in the deposition. At low pressure, clearly silane can and does diffuse back into the plasma zone. However, since the mean free path of silyl radicals at these pressures is low (of the order of 1 cm or lower) these radicals do not play a role in growth on the substrate. Rather, the silyl radicals generated near the substrate by the fractionalization of silane upon reaction with either H or excited He give rise to growth, as explained in the section of growth chemistry.

The entire ECR system is pumped by a turbomolecular pump, even during growth. The base vacuum is in the 3 to 5E-8 Torr range. The gases for doping are introduced near the substrate through a separate manifold. This way, cross contamination of the i-layer by dopant gases flowing through the same manifold is avoided. Thus, we have three manifolds, one for the plasma gases, one for the i-layer gases, and one for the dopant gases. Each manifold has a valve near the system which is cutoff so that cross-contamination between manifolds is avoided. Such cross contamination can lead to severe problems when making devices.

The substrate is tightly mounted on a polished substrate holder with a thick stainless steel mask, and heated by heating up the substrate block from the outside (using calibrated versus the heated block temperature curve), and generally the substrate temperature is about 30-40$^{\circ}$C lower than the block temperature for typical pressure, gas flow and plasma conditions we use.

## B. PECVD Processing

One hundred percent (undiluted) silane gas ($SiH_4$) is used as the process gas for all the amorphous silicon films. For most of the processing $SiH_4$ is diluted inside the deposition chamber with hydrogen. Ten percent germane ($GeH_4$) in hydrogen is used to create the alloy. The concentration of each atomic species incorporated into the material depends on the gas flow ratios of the precursor gases into the chamber, which is monitored by mass flow controllers. All of the depositions are done at low temperature(<400°C) to prevent thermally activated deposition. The substrate is heated to increase the mobility of hydrogen at the surface, which increases the passivation of dangling bond defects. Also, the thermal energy supplied to the growing surface helps to reduce the number of weak silicon bonds incorporated into the amorphous network by breaking these bonds before they become buried. The effects of temperature on growth of amorphous Si,Ge, though, has not been well characterized in the literature.

All the films for material characterization was deposited on cleaned 7059 corning glass substrates. The cleaning procedure of the substrates, consisted of boiling for ten minutes in detergent followed by the boiling in acetone and methanol solutions for five minutes each.

Once the substrates are loaded into the reactor chamber, a system cleaning process is initiated. The chamber is first pumped out with mechanical pump and then by the turbo pump through the gate valve. Then a series of gas purges with nitrogen, argon and silane are done to help remove any remaining moisture from the system. The substrate is then heated to a temperature that is at least 50°C higher than the intended deposition temperature to include outgassing of impurities from substrate and its holder.

A cleaning plasma is then lit immediately using silane and hydrogen. This cleaning plasma will etch impurities from the chamber walls and deposit a fresh layer of a-Si:H on all surfaces. A shutter is placed between the plasma and substrate to prevent deposition on the

substrate. During the last few minutes before deposition begins the $GeH_4$ is introduced in the desired proportion, in the plasma. After the plasma cleaning is completed, the film or device deposition can begin.

## C. Metalization

To measure the electrical properties of the films, metal contacts are evaporated on to the samples by a thermal evaporator. The evaporator system consists of a diffusion pumped bell jar with resistively heated tungsten metal boats. The bell jar is pumped to a base pressure of less than 2.0E-06 torr range before evaporation is started.

All of these coplanar contacts for the films are made with chromium deposited through a mask (see Figure 2.6), that produces the desired L/W ratio of 20. The chromium layer is approximately 800°A angstrom thick as measured by a thickness monitor inside the evaporator. Silver paint is applied to the top of Cr contacts to provide a good contact to the metal probe and to reduce the contact resistance. Samples are then annealed at 170°C for at least 30 minutes.

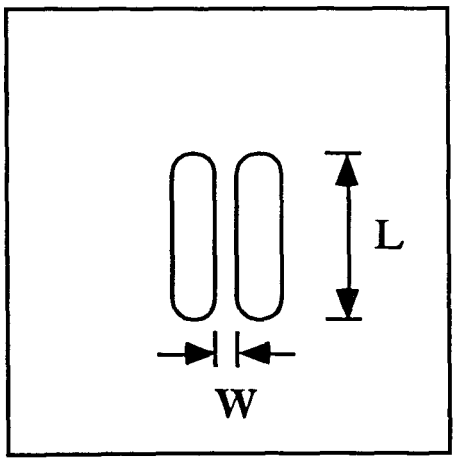


Figure 2.6. Metal mask used to evaporate contacts on the films.

# III. CHARACTERIZATION

## A. Film Thickness

The thickness of the semiconductor films deposited on glass substrates were measured using two different techniques. Primarily all of the film thicknesses were measured using a Lambda-9 dual beam spectrophotometer. The interference peaks measured over the wavelength range of 1000 nm to 2500 nm were used to calculate the thickness using the following relationship

$$t = \frac{\lambda_1 \lambda_2}{\beta n(\lambda_1 - \lambda_2)} \tag{3.1}$$

where $\beta$=2 for peak to peak intervals and $\beta$=4 for peak to valley intervals. The refractive index n of the film was found out from reflection spectra using the following relationship:

$$n = \sqrt{n_s n_a \frac{1 + \frac{n_s - n_a}{n_s + n_a}\sqrt{\frac{R_{max}}{R_{min}}}}{1 - \frac{n_s - n_a}{n_s + n_a}\sqrt{\frac{R_{max}}{R_{min}}}}} \tag{3.2}$$

where $n_a$ is the refractive index of air, $n_s$ is the reflectance of a maxima and a minima in the non-absorbing region (1000 nm $< \lambda <$ 2500 nm). The index of refraction n will vary with the Ge content and is assumed constant over the range of the wavelength used. Because of the above assumption the thickness measured is accurate only to about $\pm$ 0.1$\mu$m.

We also used a Sloan Dektak Stylus to cross-check the optical thickness measurements on several of our samples. Good agreement between the two methods was obtained.

### B. Photo and Dark Conductivity

Because they are both important and easy to measure, photo and dark conductivities ($\sigma_l$ and $\sigma_d$) are usually amongst the first set of properties measured, to characterize the electronic quality of the films.

Free carriers (electrons and holes) in a semiconductor reach their thermal equilibrium concentrations through a balance between the thermal generation and recombination processes. These free carriers with equilibrium concentrations $n_o$ and $p_o$ contribute to the conductivity of the material as,

$$\sigma = qn_o\mu_n + qp_o\mu_p \tag{3.3}$$

where $\mu_n$ and $\mu_p$ are electron and hole mobilities respectively. An estimate of the position of Fermi level can be made from the temperature dependence of conductivity. The formula for $\sigma(T)$ can be obtained from the Fermi statistics for electrons and holes densities as

$$\sigma_{n,p} = \sigma_o \exp\left[\frac{-\left(E_{c,v} - E_{fn,p}\right)}{KT}\right] \tag{3.4}$$

where $E_{c,v}$ is the conduction or valence band edge defined by the mobility gap, $E_{fn,p}$ is the quasi-Fermi level and $\sigma_O$ is the conductivity prefactor known as the minimum metallic conductivity. The above approximation is true if the mobility is only a weak function of temperature and if the presence of deep levels does not alter the occupation of band states too

severely. The Fermi energy $E_f$ can be extracted from an Arrhenius plot of the logarithm of the conductivity over a temperature range (80 to 200°C). A linear plot of $\log\sigma$ vs. $T^{-1}$ could indicate either band-like conduction beyond a sharp mobility edge or phonon-assisted hopping between nearest-neighboring localized states. Alternatively, a concave upward $\log\sigma$ vs. $T^{-1}$ plot could reflect either the absence of a sharp mobility edge or the predominance of variable-range hopping conduction. The upper limit of temperature is kept below 200°C to limit changes in band structure. Also, to prevent the photogeneration of charge carriers, the above measurement is performed in a closed dark environment.

Photoconductivity occurs when carriers are optically excited from non-conducting to conducting states. It relates to the photogeneration, transport and recombination of electrons and holes. The illumination excites electrons and holes to the band edges where they drift towards electrodes under the applied field. Photoconductivity normalized against the actual amount of light absorption is equal to the product of the quantum efficiency, mobility and recombination lifetime ($\eta\mu\tau$) for majority carriers.

The ratio of room temperature photo and dark conductivity known as photosensitivity is also an important measurement for finding out the film property. Photo and dark conductivity measurements were made in a setup designed here at the Microelectronics Research Center (MRC). To measure photoconductivity the sample is placed on the base and the probes are connected to the sample contacts. A voltage of 100V is applied across the sample. The photo and dark conductivity is determined using the following relation:

$$\sigma_{d,l} = \left(\frac{W}{L}\right)\frac{I}{V \cdot d} \qquad (3.5)$$

where (L/W) is the length to width ratio of the metal contact which in our case is 20, 'd' is the thickness of the film and V (=100V) is the applied voltage across the contacts. Since the light intensity is the same for all samples, the photosensitivity is an indication of how well the material can collect the photogenerated carriers.

## C. Sub Band Gap Absorption

Sub band gap absorption measurement can be used to get a first hand idea of the quality of films. The curve of absorption coefficient $\alpha$ versus photon energy $h\nu$ yields a joint valence band-conduction band density of states, when one makes the usual assumption that the matrix element for absorption is independent of $h\nu$. However, for use of this technique to obtain the information about sub-gap states requires the measurement of low $\alpha$ (0.1 to $10cm^{-1}$). In amorphous semiconductors such as a-Si:H alloys which are usually prepared as thin films of thickness on the order of $10\mu m$ or less, the thin film geometry limits the accurate determination of $\alpha$ from optical transmission and reflection data to $\alpha \geq 10cm^{-1}$. Thus in such cases indirect measurements that determine the spectral absorption - such as electroabsorption, photoacoustic spectroscopy (PAS), photothermal deflection spectroscopy (PDS), and constant photocurrent method (CPM) have greater sensitivities to determine the defect state densities. Amongst these PDS is the most commonly used technique. But PDS is very surface sensitive, which is a severe disadvantage if the behavior of the surface is different from that of the bulk.

To measure sub-gap absorption coefficient $\alpha$ we have used a two-beam photoconductivity technique developed by Wronski and co-workers [32]. This approach involves the use of a high intensity dc beam of light which is always incident on the on the sample and a second low intensity ac light source. The dc beam continuously creates electron-hole pairs that keep the midgap states (traps) filled and keeps the occupancy of the mid gap states unchanged. The ac beam superimposes on the dc beam and thus modulates the

photocurrent generated in the sample by creating additional electron-hole pairs. The change in photocurrent produced in the sample as we change the energy of this ac beam can be detected by a lock in amplifier and can be related to the absorption co-efficient of the film.

The schematic of the apparatus is as shown in Figure 3.1. In this set up, the monochrometer is used to change the wavelength of the incident photons. The range of wavelength that is incident on the sample in this measurement is from 600nm to 1100nm. The output of the monochrometer is chopped.

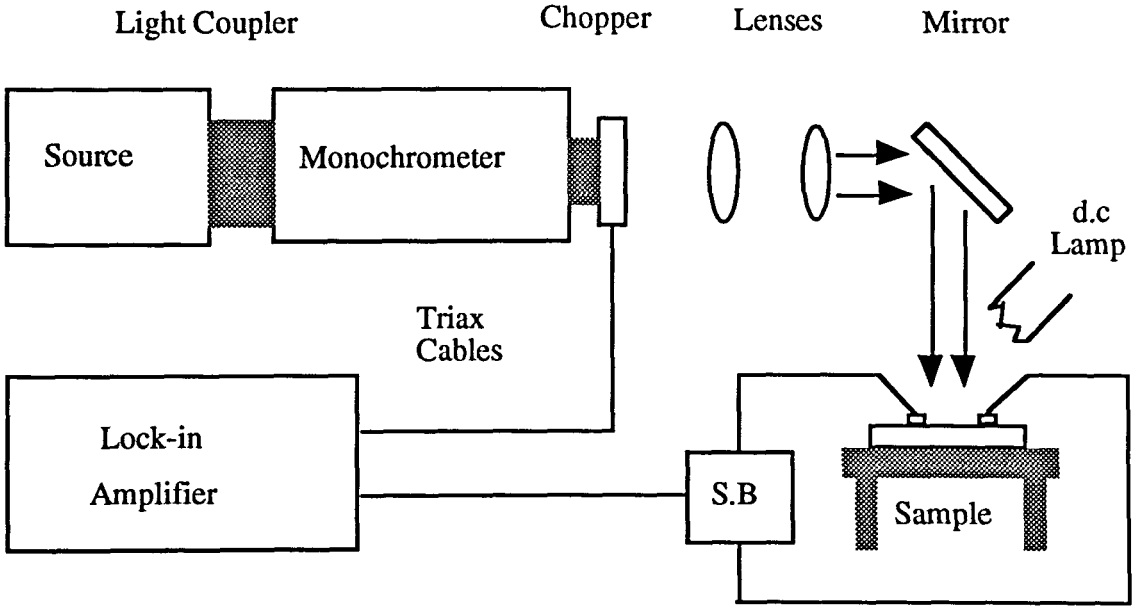


Figure 3.1. Apparatus for measuring sub-bandgap a using two-beam photocurrent technique.

The chopped beam is focused onto the sample through a beam splitter, the other half of which goes to a photodetector used as a reference cell. This reference cell is used to determine the photon flux incident on the sample at each wavelength. The chopper modulates the photon signal to produce a 13.5Hz square wave. This operation reduces the noise due to the ambient light and 60Hz power lines. A high pass filter is also used at $\lambda \geq 700$nm to get rid of photons of lower wavelength. The sample is provided with coplanar contacts, usually of Cr or Ti. To minimize errors due to scattering etc., the contacts are 0.2mm apart. The sample is provided with a dc bias voltage of 20V, and the ac current through the sample is detected using a tuned pre-amplifier and a lock-in amplifier. Since the lifetime of the sample is constant (because of dc light with intensity of about 0.1 mW/cm$^2$), the photocurrent should correspond directly to the absorption coefficient $\alpha$. To calibrate the apparatus, we have measured some standard glow discharge produced films provided by Dr. Wronski, along with his measured $\alpha$ curves. Since the absorption of each film is different, we calibrate each film by comparing the photo-conductivity absorption of the films in the region 1E3/cm<$\alpha$<5E3/cm with the absorption from the spectrophotometer. Note that the calibration procedure needs to take account of the fact that photo-conductivity absorption depends on the assumption that the photons are absorbed uniformly in the material, but the spectro-photometric $\alpha$ does not. The complete procedure to derive the correction factor is shown in Appendix B.

## D. Infrared Measurements

Infrared (IR) absorption measurements of the vibrational modes yield important information on a-Si:H and a-Ge:H. The peak positions indicate the bonding configurations of the hydrogen atoms as well as oxygen or nitrogen impurity contamination. The integration over certain peaks yields information on the hydrogen concentration. A single beam Fourier

Transform Infrared (FTIR) spectrometer, IBM model IR98, was used in our measurements. All samples used in the IR measurements were deposited on lightly doped single crystal crystal silicon. Other unused pieces from the same wafer substrarte were used as the reference.

A variety of vibrational modes are observed in the IR spectra of a-Si:H and a-Ge:H. The major vibrational modes for hydrogen in a-Si:H were identified by Brodsky et al [33]. The corresponding bonding configurations are dipicted in Figure 3.2. The three modes are (1) the Si-H stretching mode (2000-2100 $cm^{-1}$), (2) the Si-$H_2$ and Si-$H_3$ bond bending scissors mode (840-890 $cm^{-1}$), and (3) the Si-H wagging mode (640 $cm^{-1}$). The absorption peaks in a-Ge:H, are at slightly lower frequencies, mainly due to the higher atomic mass of Ge. They are at 1870-1970, 780, and 580 $cm^{-1}$ respectively. The deuterium-related peaks are similarly at lower frequencies. If the hydrogen content is low, the absorption intensity will usually be weaker than the interference fringes, which complicates the qualitative analysis.

The Si (or Ge) bonded H content is determined from the integrated intensity of the 640 (580) $cm^{-1}$ wagging mode, using calibration coefficient provided by Shanks et al. [34] and Catherine et al. [35]. The coefficient was shown to be insensitive to the bonding configuration and microstructure in a-Si:H, and is believed to be similarly insensitive in a-Ge:H as well. The hydrogen content determined from this absorption peak is consequently believed to be reliable. The equation used to calculate the hydrogen content is given by Cardona [36-37]:

$$N_H = A\int \frac{\alpha(\omega)}{\omega} d\omega \qquad (3.6)$$

where A is an experimentally determined constant, and $\alpha(\omega)$ is the absorption coefficient at angular frequency $\omega$. The integral extends over the absorption band of interest. The values of A for the vibrational modes in Si andGe are listed in Table 3.1.

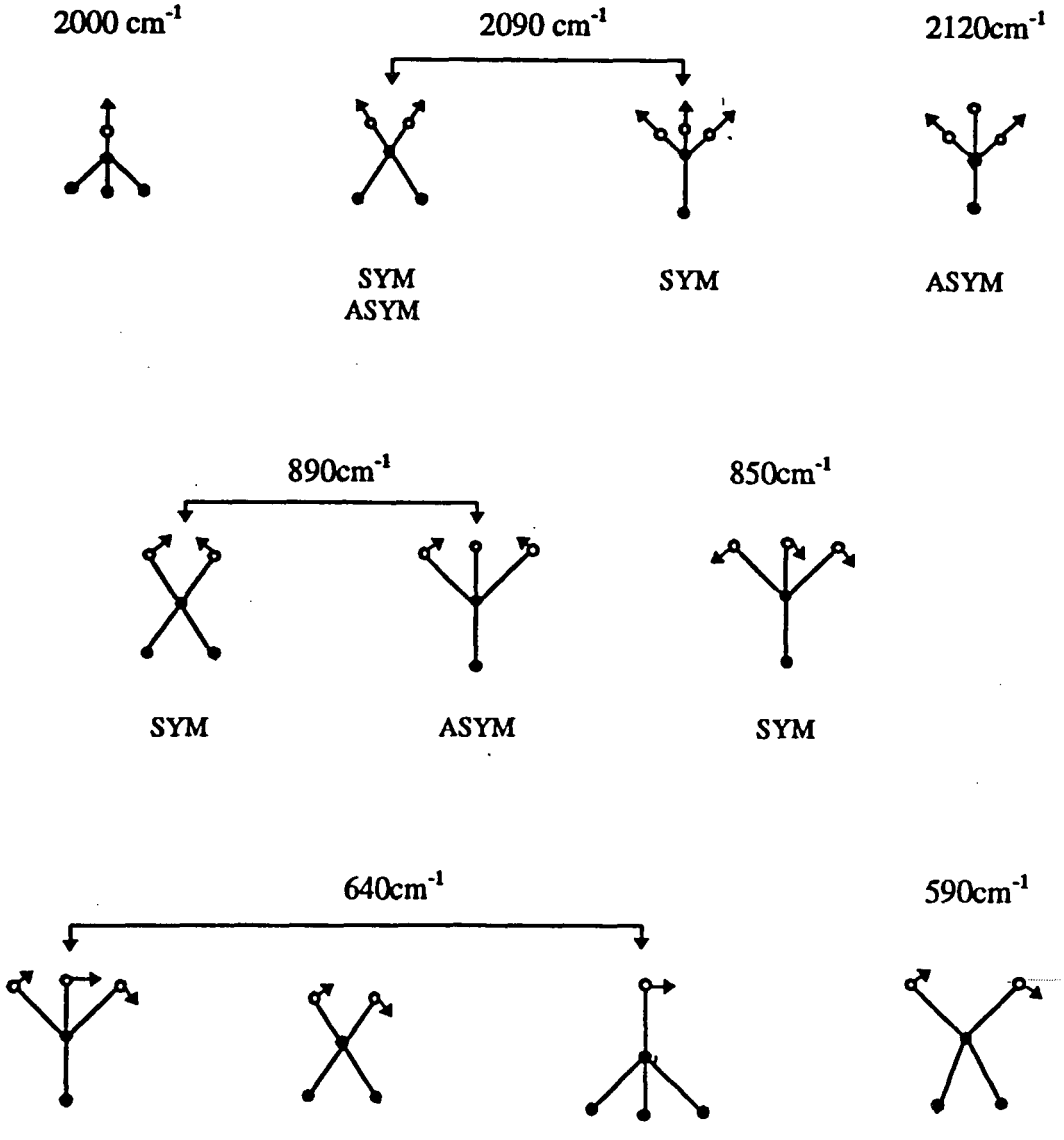


Figure 3.2. Schematic illustration of the bond stretching (top row), bond bending (middle r-ow), and bond wagging and rocking (bottom row) modes of SiH, $SiH_2$, and $SiH_3$. SYM and ASYM indicates symmetric and asymmetric modes respectively. The solid and open circles represent Si and H atoms respectively [33].

Table 3.1 The various vibrational modes of hydrogen in a-Si:H and a-Ge:H, their bonding configurations and the corresponding proportionality constant A [34-37].

**For a-Si:H**

| Wavenumber ($cm^{-1}$) | 640 | 840-890 | 2000 | 2100 | 2100 |
|---|---|---|---|---|---|
| Mode | Wag | Scissors | Stretch | Stretch | Stretch |
| Bonding | Si-H<br>$Si-H_2$<br>$Si-H_3$ | Si-H | Si-H<br>(Isolated) | Si-H<br>(Clustered) | $Si-H_2$<br>$Si-H_3$ |
| A ($cm^{-1}$) ($10^{19}$) | 1.6 | 20 | 2.2 | 17 | 9.1 |

**For a-Ge:H**

| Wavenumber ($cm^{-1}$) | 565-575 | 760-825 | 1875-1895 | 1960-1970 |
|---|---|---|---|---|
| Mode | Wag | Scissors | Stretch | Stretch |
| Bonding | Ge-H<br>$Ge-H_2$ | $Ge-H_2$ | Ge-H | $Ge-H_2$ |
| A ($cm^{-1}$) ($10^{19}$) | 1.1 | | 5.0 | 14 |

The following expression gives the hydrogen concentration $C_H$ in a-Si:H:

$$C_H(at.\%) = 1.125\frac{S_{640}}{d} \tag{3.7}$$

where$S_{640}$ is the area (in $cm^{-1}$) under the 640 cm-1 absorption peak and d is the thickness in microns. Similarly, for a-Ge:H

$$C_H(at.\%) = 1.0\frac{S_{580}}{d} \tag{3.8}$$

where$S_{580}$ is the area (in $cm^{-1}$) under the 580 cm-1 absorption peak. The atomic percentage of Si in Si-$H_2$ and Si-$H_3$ is given by

$$N_d(at.\%) = 10.44\frac{S_{840}}{d} \tag{3.9}$$

and that of Ge-$H_2$ and Ge-$H_3$ is given by

$$N_d(at.\%) = 11.5\frac{S_{780}}{d} \tag{3.10}$$

# IV. RESULTS

To determine the electronic properties of the alloyed material, a series of a-(Si,Ge):H films were grown on 7059 glass with the deposition conditions listed in the Table 4.1. Also for comparison, the results from the characterization of the similar material grown using Glow discharge by previous workers have been used. Two set of a-(Si,Ge):H films were grown, one with hydrogen dilution and the other using helium dilution. Typical dilution ratio of He to the mixture of $SiH_4$ and $GeH_4$ was about 15:1. The growth rates were between 1-1.5°A/sec. Some pure a-Si:H films were also grown with the deposition conditions listed in Table 4.1, for comparing the properties of pure a-Si:H with the a-(Si,Ge):H alloys.

The electrical and optical characteristics of these films are listed in Table 4.2. The Tauc gap energies are found from the Tauc plots discussed in chapter 2. As expected the Tauc bandgap decreases with the increase in the germanium content in the films. The substrate temperature during deposition also seems to affect the bandgap. This is consistent with the idea that the substrate temperature during growth affects the hydrogen content in the film; increased temperature results in lower hydrogen content and lower $E_g$. However, the H and Ge contents of a-Si,Ge:H films are not independent parameters [p29]. Fortman and Tu showed the interrelation between germanium content, temperature, hydrogen content, and optical bandgap.

The activation or Fermi energy values of the films were near the center of the Tauc gap. This indicates that the films are more or less intrinsic. The growth rates listed in Table 4.2 are highly consistent, with small increases at increased plasma power levels and small decreases with higher levels of hydrogen dilution. Hydrogen dilution is known to lower the growth rate by reducing the mean free path of the reactive $SiH_X$ molecules and by etching the sample

Table 4.1. Deposition conditions of a-(Si,Ge):H films used for optical and electrical characterization.

| | | | | | Gas Flow Rates | | | |
|---|---|---|---|---|---|---|---|---|
| | | | | | 100% | 10% | 100% | 100% |
| | Pressure | Temp. | Power | Time | $SiH_4$ | $GeH_4$ | $H_2$ | He |
| Sample# | (mTorr) | (°C) | (watts) | (min) | (%) | (%) | (%) | (%) |
| 2/1126 | 10 | 350 | 45 | 120 | 40.0 | 6.0 | - | 100 |
| 2/1128 | 10 | 350 | 40 | 90 | 26.0 | 6.0 | - | 100 |
| 2/1129 | 10 | 350 | 40 | 90 | 40.0 | 6.0 | - | 100 |
| 2/1132 | 10 | 350 | 40 | 90 | 22.0 | 6.0 | - | 100 |
| 2/1135 | 10 | 350 | 45 | 100 | 20.0 | 7.0 | - | 100 |
| 2/1249 | 10 | 350 | 25 | 120 | 20.0 | 7.0 | - | 100 |
| 2/1275 | 10 | 300 | 30 | 85 | 30.0 | 7.0 | - | 100 |
| 2/1280 | 10 | 300 | 30 | 75 | 40.0 | 5.0 | - | 100 |
| 2/1331 | 10 | 350 | 120 | 126 | 20.0 | 6.0 | 20.0 | - |
| 2/1332* | 10 | 350 | 120 | 135 | 20.0 | 6.0 | 20.0 | - |
| 2/1334 | 10 | 350 | 120 | 120 | 20.0 | 4.0 | 20.0 | - |
| 2/1335* | 10 | 350 | 120 | 145 | 20.0 | 4.0 | 20.0 | - |
| 2/1339 | 10 | 350 | 120 | 148 | 25.0 | 4.0 | 20.0 | - |
| 2/1343* | 10 | 300 | 120 | 138 | 20.0 | 4.0 | 20.0 | - |

**Note:** * in the sample column indicates that 10% of 10ppm diborane was used during deposition.

Table 4.2. Material characteristics

| Sample# | Thickness (μm) | Tauc gap (eV) | $\sigma_d$ (S/cm) | $\sigma_{ph}$ (S/cm) | Photosens. ($\sigma_{ph}/\sigma_d$) | Growth rate (°A/sec) | α ($cm^{-1}$) |
|---|---|---|---|---|---|---|---|
| 2/1126 | 1.66 | 1.53 | 1.64e-10 | 4.2e-6 | 2.5e+4 | 2.3 | 0.5 |
| 2/1128 | 0.80 | 1.47 | 2.6e-10 | 4.6e-6 | 1.7e+4 | 1.48 | 0.9 |
| 2/1129 | 1.01 | 1.54 | 2.2e-10 | 6.8e-6 | 3.0e+4 | 1.87 | 0.3 |
| 2/1132 | 0.75 | 1.47 | 6.0e-10 | 4.0e-6 | 6.7e+3 | 1.39 | 0.8 |
| 2/1135 | 0.81 | 1.44 | 6.0e-10 | 3.4e-6 | 5.7e+3 | 1.35 | 0.9 |
| 2/1249 | 1.50 | 1.41 | 1.0e-9 | 3.30e-6 | 3.3e+3 | 2.08 | 0.8 |
| 2/1275 | 1.15 | 1.49 | 6.0e-10 | 5.0e-6 | 8.3e+3 | 2.25 | 1.0 |
| 2/1280 | 1.05 | 1.56 | 3.0e-10 | 8.3e-6 | 1.0e+4 | 2.33 | 1.3 |
| 2/1331 | 0.96 | 1.39 | 1.15e-8 | 1.7e-5 | 1.5e+3 | 1.27 | - |
| 2/1332* | 1.03 | 1.39 | 5.1e-9 | 1.12e-5 | 2.2e+3 | 1.27 | - |
| 2/1334 | 0.83 | 1.43 | 1.51e-9 | 1.93e-5 | 1.3e+4 | 1.16 | 0.9 |
| 2/1335* | 1.06 | 1.44 | 9.4e-10 | 9.43e-6 | 1.0e+4 | 1.22 | .85 |
| 2/1339 | 1.14 | 1.47 | 8.77e-10 | 1.62e-5 | 1.8e+4 | 1.29 | - |
| 2/1343* | 1.12 | 1.43 | 2.99e-9 | 3.04e-5 | 1.0e+4 | 1.35 | 0.8 |

**Note:** * in the sample column indicates that 10% of 10ppm diborane was used during deposition.

surface. This surface etching is beneficial since weakly bonded silicon is removed before it becomes incorporated in to the material.

The dark and photoconductivity results are plotted in Figures 4.1 and 4.2 respectively as functions of the Tauc gap. Upon comparing these with the results discussed in chapter 2, it is obvious that we have succeeded in getting a very good control over our film properties. As found out by most researchers, the photoconductivity of the material decreases and dark conductivity increases as the Tauc gap decreases (with increasing germanium content). We also see that the decrease in photoconductivity is gradual and systematic. In Figure 4.4 for comparison we have plotted the photoconductivity of the films grown by GD and ECR CVD as the function of the Tauc gap. It can be clearly seen that for a given Tauc gap, the photoconductivity of the films grown by ECR CVD have a higher value than that of the ones grown using GD technique. This indicates that we are able to grow a better material using ECR technique. Also from the Figure 4.3 it is clear that helium dilution gives a better material than one deposited using hydrogen dilution. This indicates that with helium dilution, we are able to achieve a lower Tauc gap with less germanium content in the film. The above speculation is based on the fact that germanium introduces new midgap defects that reduce the photo generated carrier lifetime.

Another important parameter to judge the material quality is the ratio of photo to dark conductivity known as photosensitivity. Figure 4.3 shows that as expected, the photosensitivity values decrease with decrease in the Tauc gap (with increase in germanium content). The drop in photosensitivity is not severe, which provides the first indication that the silicon-germanium films are device quality. Previous photosensitivity data reported in the literature indicate that a-(Si,Ge):H films can have a wide range of values for the photo and dark conductivity. Both parameters often vary over several orders of magnitude at a particular value for the germanium content. Thus our consistent results indicates that high quality material can be deposited on a reproducible basis using ECR CVD.

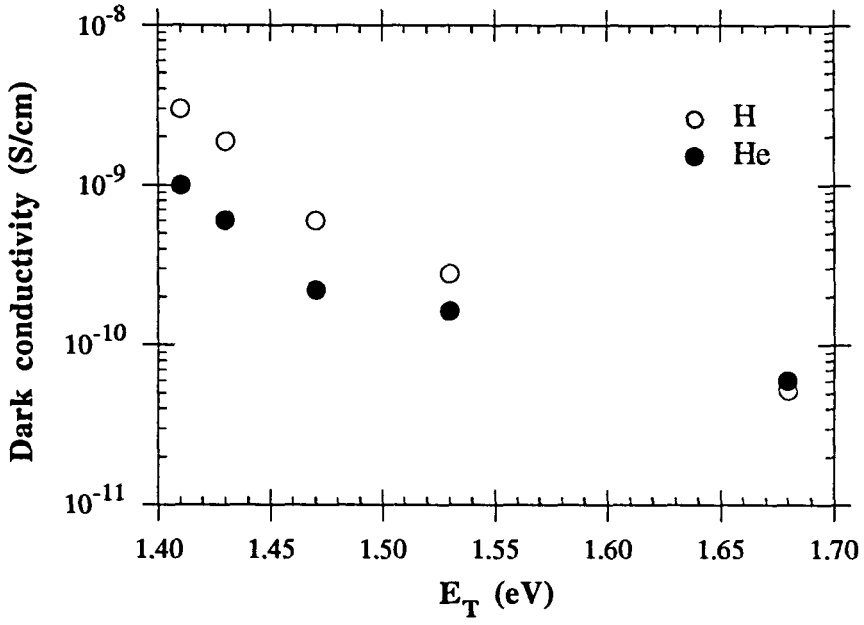


Figure 4.1. Dark-conductivity dependence on Tauc gap for a-(Si,Ge):H films.

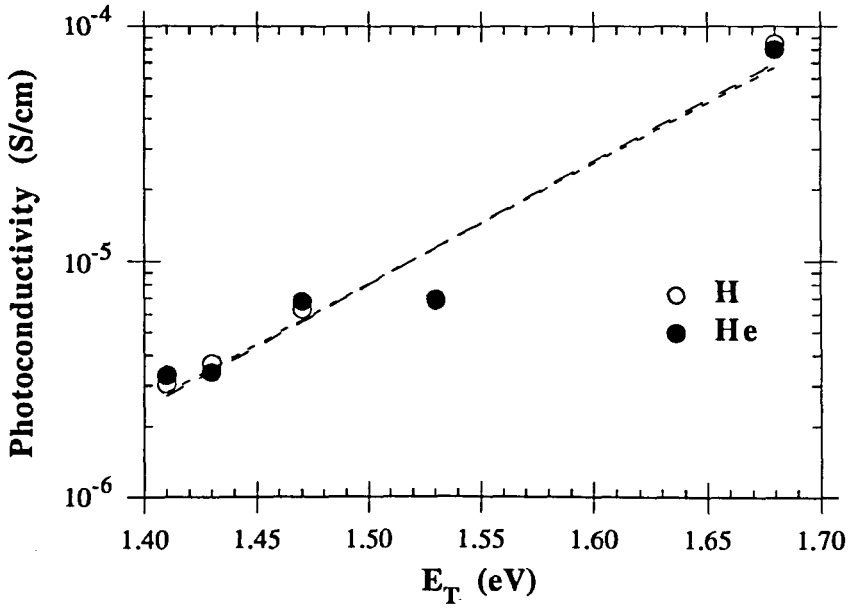


Figure 4.2. Photo-conductivity dependence on Tauc gap for a-(Si,Ge):H films.

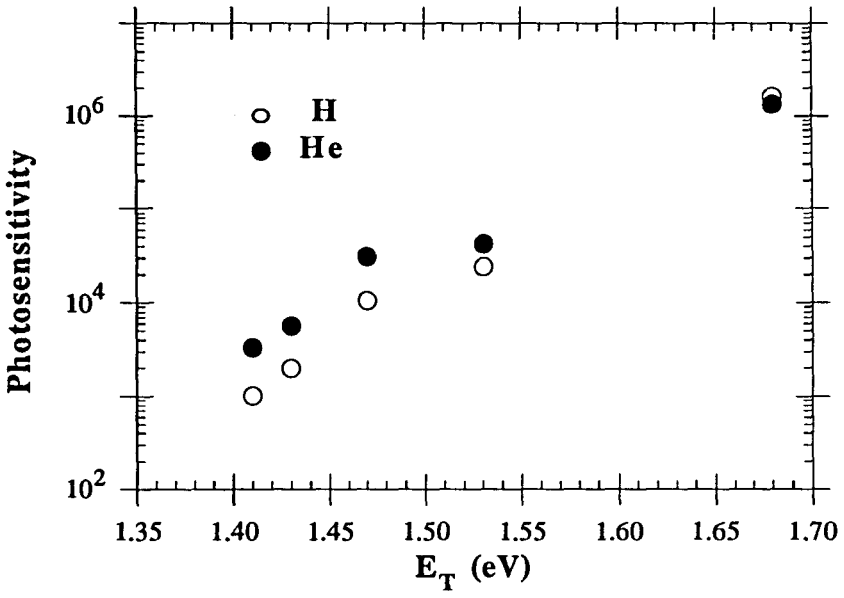


Figure 4.3. The effect of the Tauc gap on photosensitivities of a-(Si,Ge):H films.

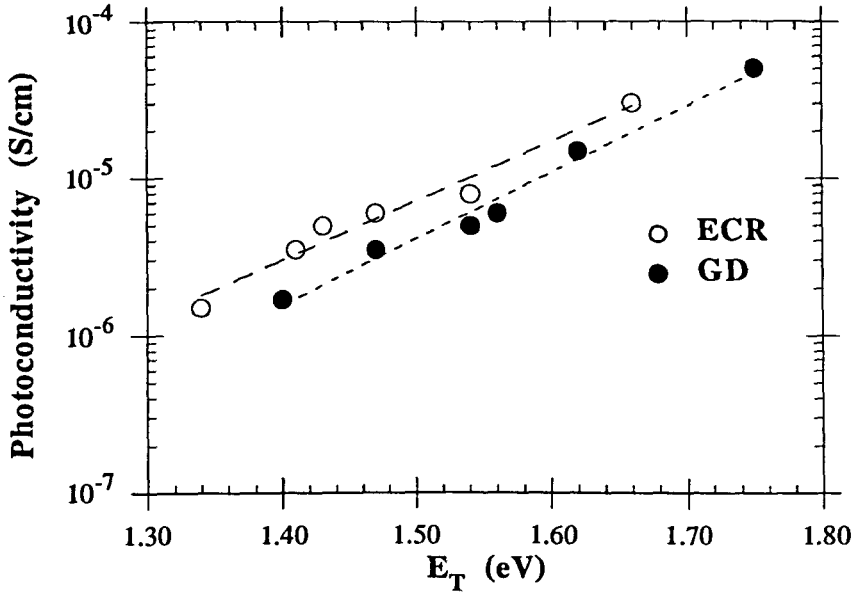


Figure 4.4. Comparision of Photo-conductivity dependence on Tauc gap for a-(Si,Ge):H films grown using two different growth techniques.

Another property that we measured was the sub gap absorption of the film. This was measured using a two beam photo-conductivity technique. Photon absorption in this sub gap energy range is due to the presence of energy states within the Tauc gap. Low values for the absorption coefficient ($\leq$ 3.0 $cm^{-1}$) are indicative of low defect densities. The sub-gap absorption coefficient '$\alpha$' used for this measurement is found from the knee of the absorption data from the films. $\alpha$ measured at the shoulder of the sub gap absorption plot for different films is plotted as a function of Tauc gap in Figure 4.5. Once again, in accordance with the results shown in Figures 4.1 and 4.2, the sub gap $\alpha$, which is a measure of mid-gap defect densities, does not increase precipitously as we increase the Ge content of the film; rather, the increase is gradual and systematic.

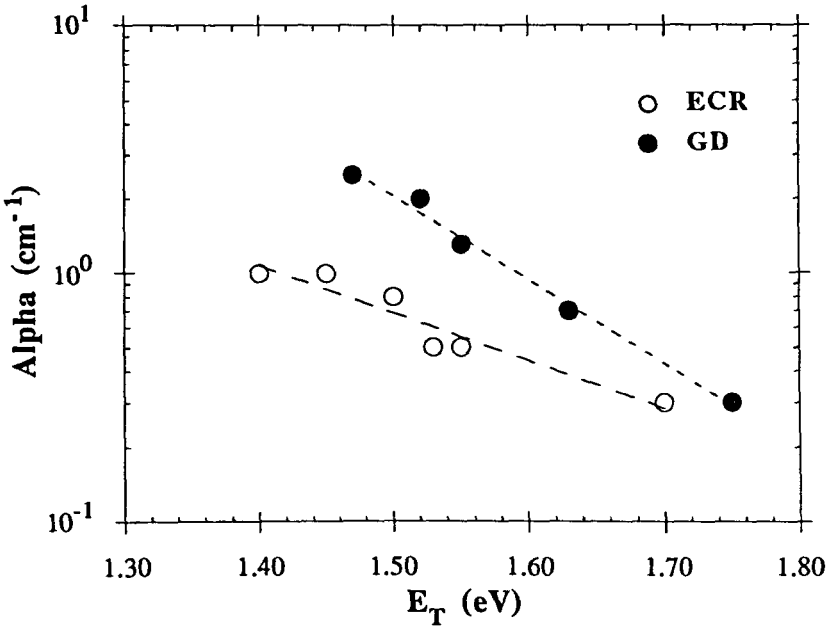


Figure.4.5. Sub gap a at the shoulder vs.Tauc gap for a-(Si,Ge):H films deposited using ECR and GD techniques.

Figure 4.5 shows a comparison of the sub gap α for the films grown using ECR and GD techniques. It is again clear that the films grown by ECR CVD have a smaller α for a given Tauc gap, as compared to the films grown using GD CVD. This reconfirms our belief that an alternative technique like ECR CVD can be used to grow a better quality a-(Si,Ge):H material.

The next parameter that can be measured using sub gap photo-conductivity techniques is the Urbach energy of the films. As explained earlier, this measurement is an indication of material quality since the Urbach energy closely follows the slope of the valence band tail states. Higher values for the Urbach energy indicate broader valence band tails and larger defect densities. The results of Figure 4.6 clearly show that the Urbach energy does depend on the germanium content. In fact it increases with the decrease in Tauc gap (increase in germanium content).

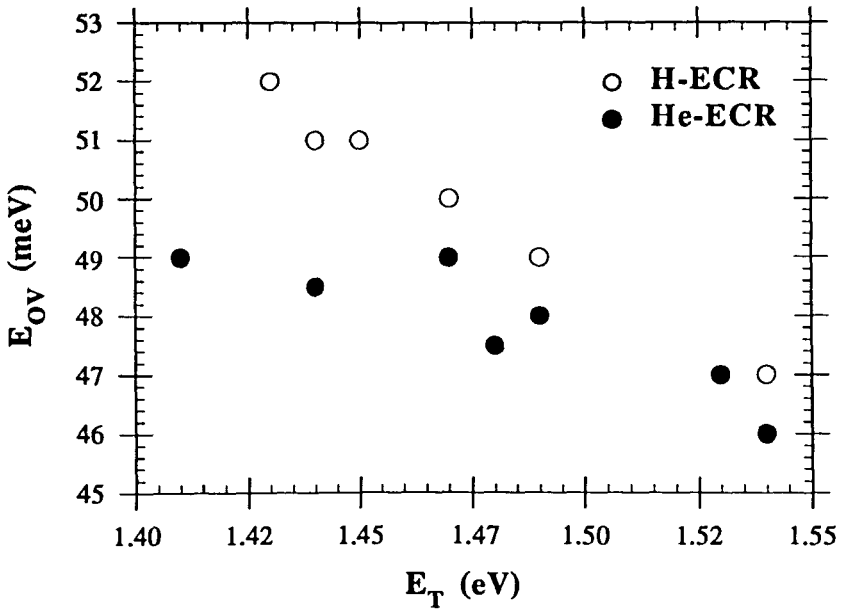


Figure 4.6. Dependence of the Urbach energy on the tauc gap of a-(Si,Ge):H films.

Figure 4.6 also indicates that, the Helium diluted films grown using ECR technique had low Urbach energies as compared to the films grown with hydrogen dilution for a given Tauc gap.This indicates that ion bombardment by He ions produced by the intense ECR discharge, when combined with a high dilution ratio to prevent gas phase reactions, leads to improvements in the film properties such as disorder and sub gap $\alpha$. Figure 4.7 shows a plot of Urbach energy vs Tauc gap for the films grown using ECR and GD CVD techniques. We also observe that the values of Urbach energies were lower than for comparable films using triode GD CVD technique.

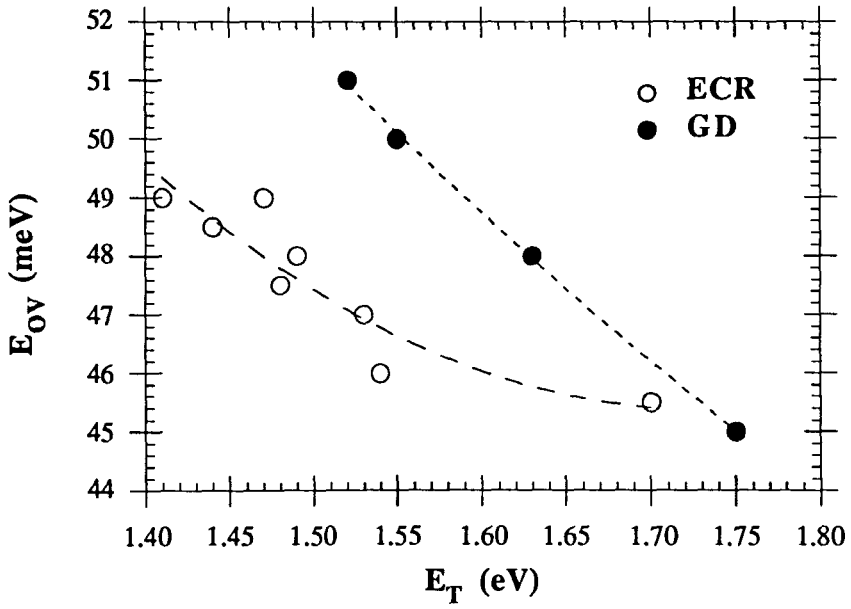


Figure 4.7. Urbach energy of ECR and GD-deposited a-(Si,Ge):H films.

It is worthwhile to study the product of photoconductivity and sub gap $\alpha$ at the shoulder, and plot this product as a function of the Tauc gap (Ge content). Since the sub gap $\alpha$ is a measure of the midgap defect density, and presumably an increase in defect density will lead to a decrease in electron $\mu\tau$ product (and hence in photoconductivity), the product of these quantities, when plotted vs. Tauc gap, will tell us if the mid gap defects are the controlling factors in the photoconductivity. This plot is shown in Figure 4.8. From this plot, it appears that indeed, $\alpha\mu\tau$ product is constant as a function of Tauc gap, strongly suggesting that the midgap defects are controlling photoconductivity. Our results agree with the conclusion of Cohen and co-workers, who found the similar result when they plotted the product of $\mu\tau$ and defect density derived from capacitance spectroscopy on Schottky devices.

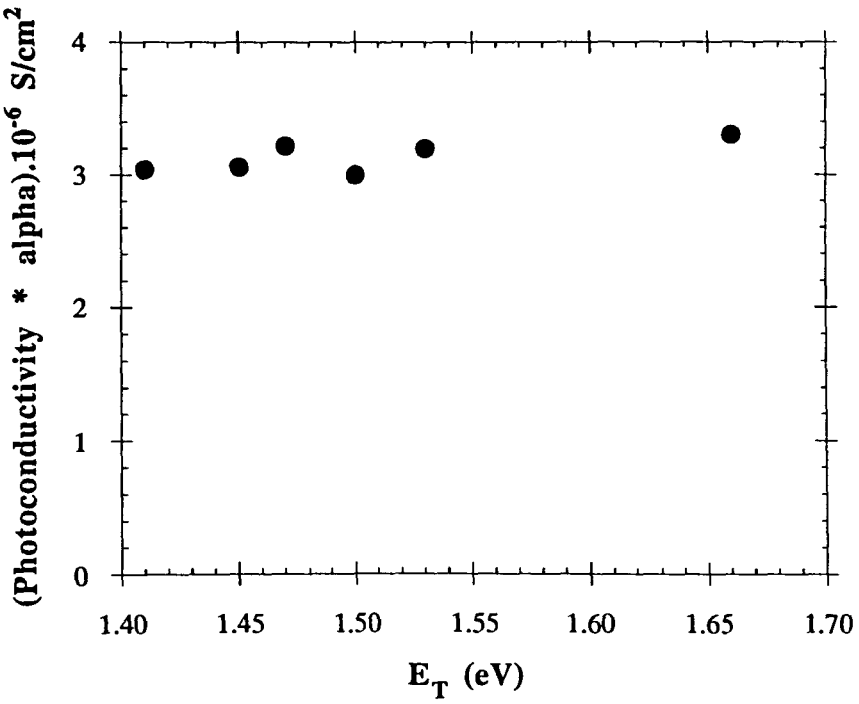


Figure 4.8. Product of $\sigma_l$ and sub-gap $\alpha$ vs. Tauc gap for ECR deposited a-(Si,Ge):H films.

To determine the hydrogen content, the films were deposited on both side polished Si wafers with resistivity ranging from 6-10 ohm-cm. The single beam Fourier Transform Infrared (FTIR) spectrometer, IBM model IR98, was used in our measurements. Blank pieces from the same wafer substrate were used as reference. Table 4.3 indicates the parameters used to grow the material for the FTIR measurements. The IR absorption spectrum for some of the films are shown in Figures 4.9 and 4.10.

Since the hydrogen content in the films were low, especially in the films deposited using He dilution, the absorption intensities were not very strong as compared to the interference fringes. This made the calculations for the area slightly less accurate, thereby

Table 4.3. Deposition conditions of a-(Si,Ge):H films used for FTIR measurements.

| | | | Gas Flow Rates | | | | | |
|---|---|---|---|---|---|---|---|---|
| | | | 100% | 10% | 100% | 100% | Tauc | |
| | Pressure | Temp. | $SiH_4$ | $GeH_4$ | $H_2$ | He | $E_g$ | $C_H$ |
| Sample# | (mTorr) | (¤C) | (%) | (%) | (%) | (%) | (eV) | (at %) |
| 2/1542 | 10 | 350 | 20.0 | 7.0 | - | 100 | 1.42 | 3.47 |
| 2/1543 | 10 | 350 | 40.0 | 7.0 | - | 100 | 1.48 | 3.94 |
| 2/1544 | 10 | 300 | 40.0 | 7.0 | - | 100 | 1.48 | 3.52 |
| 2/1545 | 10 | 350 | 20.0 | 0.0 | - | 100 | 1.70 | 4.51 |
| 2/1546 | 10 | 350 | 40.0 | 6.0 | - | 100 | 1.55 | 3.44 |
| 2/1548 | 10 | 350 | 20.0 | 4.0 | 20 | - | 1.44 | 6.63 |
| 2/1549 | 10 | 300 | 30.0 | 4.0 | 30 | - | 1.52 | 7.05 |
| 2/1550 | 10 | 300 | 20.0 | 4.0 | 20 | - | 1.42 | 6.22 |
| 2/1551 | 10 | 300 | 30.0 | 0.0 | 30 | - | 1.72 | 7.37 |

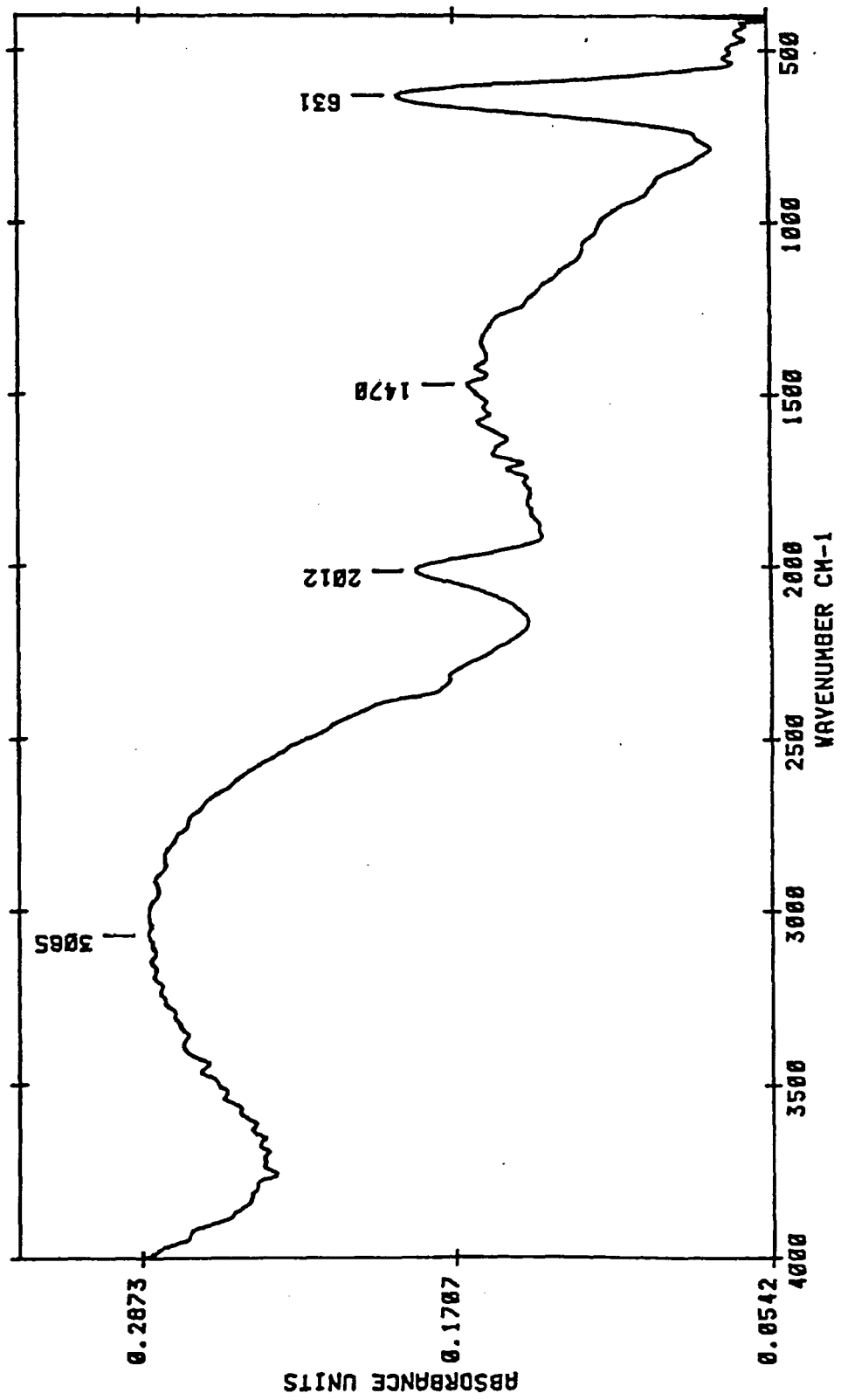


Figure 4.9. The IR absorption spectra of sample 2/1545.

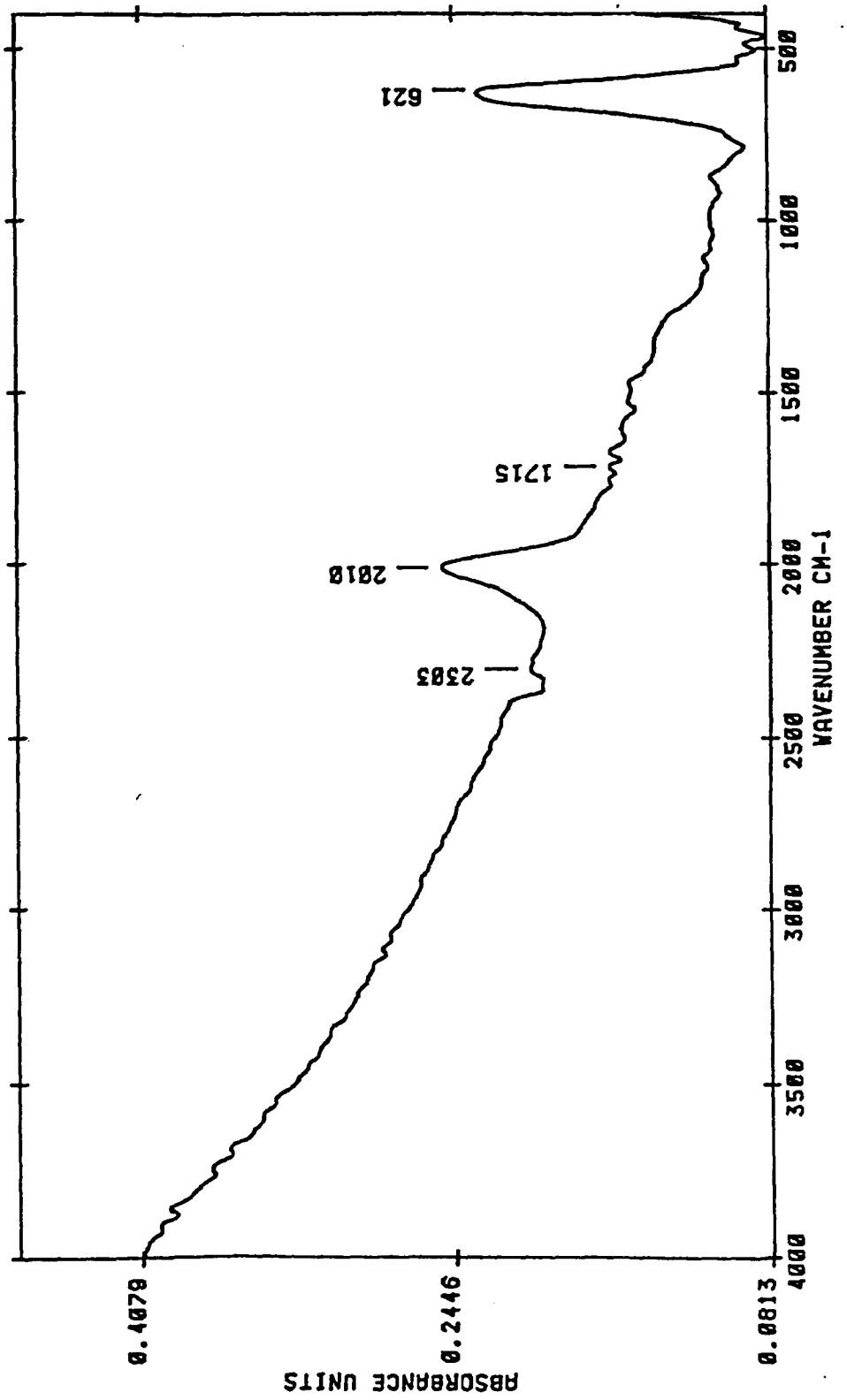


Figure 4.10. The IR absorption spectra of sample 2/1548.

giving some error in the calculation of the hydrogen concentration which was done using equation 3.7. In the Figure 4.11 we have plotted the hydrogen concentration as a function of the Tauc gap for a-(Si,Ge):H films deposited both with hydrogen and helium dilution. We observe that hydrogen content in the films grown with helium dilution is appreciably lower compared to the films deposited with hydrogen dilution.

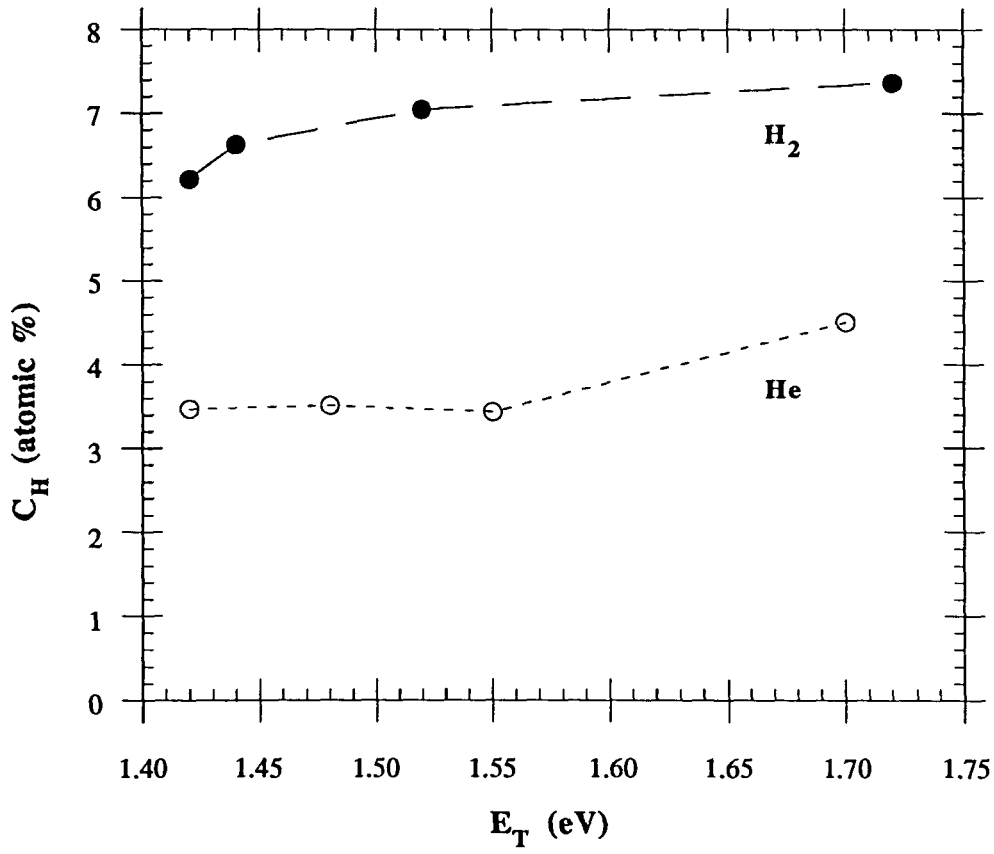


Figure 4.11. Hydrogen content as a function of Tauc gap for a-(Si,Ge):H prepared by ECR CVD with hydrogen and helium dilution.

This indicates that with He dilution it is possible to achieve a lower bandgap of the alloy material with less germanium, than needed to achieve with $H_2$ dilution. The above fact indicates that ion bombardment by He ions produced by the intense ECR discharge, can lead to improvements in the film properties such as low disorder and sub gap $\alpha$. This falls in line with all the results obtained thus far in our study of the a-(Si,Ge):H films grown using ECR PECVD technique.

We also see that the hydrogen content in the films decreases with the decrease in Tauc gap of the films (i.e. with the increase in germanium content). This is in agreement with the observations of the researchers like Mitchell et al.[1985] and Shimizu, T., et al. [1986]. One reason for this reduction in the total H content with increasing Ge content in the alloy is that the hydrogen attaches preferentially to silicon rather than to germanium [Paul, D., et al. 1980, von Roedern et al. 1982, Mackenzie et al. 1985, Ichimura et al. 1985, Guha 1985]. Paul, D. K., et al. [1980] reported preferential H attachment to Si of about 10 for various Ge contents. Sato et al. in 1988 proved that both Si-H and Ge-H bondings decrease with increasing germanium content. As a result of the preferential attachment of hydrogen to silicon rather than to germanium and the weakness of the Ge-H bonds, relatively more defects in a-(Si,Ge):H alloys are Ge dangling bonds than Si dangling bonds [Paul et al. 1981].

# V. CONCLUSIONS

We investigated the growth of a-(Si,Ge):H material using a remote plasma beam technique, using plasmas generated by electron cyclotron resonance (ECR) conditions. Both reactive (hydrogen) and the non reactive (helium) gases were used as the primary plasma gas. The reactants generated by the ECR plasma from these gases were allowed to flow towards the substrate, where they reacted with the mixture of silane and germane to give rise to the growth of a-(siege):H.

The growth temperatures were reasonably high, in the range of 300-350°C. The films were characterized using activation energy, photo-conductivity and sub-gap absorption techniques. The hydrogen content in the films was also determined using FTIR spectroscopy technique. We found that the films grown using He plasma beams had very low Urbach energies for valence band tails, and also a correspondingly low sub-gap absorption coefficient $\alpha$. The values of both subgap $\alpha$ and Urbach energies were lower than for comparable films deposited using triode-glow discharge deposition. We have carefully measured the electronic properties of the material, and have shown that the Urbach energy of the valence band tail does increase, by small but significant amount, as the Tauc gap of the films reduces (i.e. as the Ge content increases). Corresponding to this increase in Urbach energy, there is an increase in subgap absorption coefficient.

The plot of product of photoconductivity and subgap $\alpha$ at the shoulder as the function of the Tauc gap clearly indicated that indeed , $\alpha\mu\tau$ product is constant as a function of Tauc gap, strongly suggesting that the midgap defects are controlling the photoconductivity. This result was in agreement with the conclusion of Cohen and co-workers.

We also found that the use of He lead to the achieving of a lower Tauc bandgap for a given Si:Ge ratio in the solid phase than for comparable glow discharge films. Even the Tauc

bandgap of a-Si:H, deposited using He-ECR discharge was much lower (1.67eV) than that of the films deposited using H-ECR discharge (1.75eV). The corresponding H concentrations were also lower in He-ECR films, and yet the electronic properties were superior compared to a material with the same Tauc gap deposited using H. This clearly indicates that ion bombardment by He ions produced by intense ECR discharge, when combined with high dilution ratio to prevent gas phase reactions, lead to improvements in the film properties such as disorder and subgap $\alpha$. Thus we have tried to show that the chemistry of growth and deposition conditions play a major role in determining the properties of a-(Si,Ge):H thin film material.

# REFERENCES


[1] Madan, A., and Shaw, M.P., *The Physics and Application of Amorphous Semiconductors* (Academic Press Inc., San Diego, 1988).

[2] Mott, N.F., and Davis, E.A., *Electronic Processes in Non-Crystalline Materials* (Clarendon Press, Oxford, 1979).

[3] Street, R.A., *Hydrogenated Amorphous Silicon* (Cambridge University Press, Cambridge, U.K., 1991).

[4] Fritzsche, H., *Properties of Amorphous Silicon*, EMIS Datareview Series No.1,ed. (ISPEC, New York, 1989).

[5] Zachariasen, W.H., "The atomic arrangement in glass," *J. American Chemical Soc.* **104**, 3841 (1932).

[6] Mackenzie, K.D., Eggert, J.R., Leopold, D.J., Li, Y.M., Lin, S., and Paul, W., "Structural, electrical, and optical properties of a-(Si,Ge):H and an infrared band structure," *Phys. Rev. B* **31**, 2198 (1985).

[7] Paull, W., Street, R.A., and Wagner, S., "Hydrogenated amorphous semiconductors," *J. Elect. Mat* **22**, 39 (1993).

[8] Fortmann, C., Dawson, R., Gunes, M., Wronski, C., "Amorphous silicon dispersive transport considerations for analysis of films and solar cells," *J. Non-Crys. Sol.* (1994).

[9] Orenstien, J., Kastner, M., and Vaninov, V., "Transient photoconductivity and photo-induced optical absorption in amorphous semiconductors," *Phil. Mag.B* **46**, 23 (1982).

[10] Smith, R.A., *Semiconductors* (Cambridge University Press, New York, 1978).

[11] Mackenzie, K.D., Burnett, J.H., Eggret, J.R., Li, Y.M., and Paul, W., "Comparison of structural, electrical, and optical properties of amorphous silicon-germanium alloys produced from hydrides and flourides," *Phys. Rev. B* **38**, 6120 (1988).

[12] Tsuda, S., et. al., "High quality a-SiGe alloys prepared by new methods," *J. Non-Crys. Solids* **77**, 845 (1985).

[13] Nakamura, G., Sato, K., and Yukimoto, Y., "High performance tandem type amorphous solar cells," *Proc. 16th IEEE PV Spec. Conf.*, 1331 (1982).

[14] Shing, Y.H., et.al., "In situ process diagnostics of silane plasma for device-quality a-Si:H deposition," *Proc. 19th IEEE PV Spec. Conf.*, 577 (1987).

[15] Shimizu, I., "Properties of amorphous silicon based alloys prepared from fourides and hydrogen," *J. Non-Crys. Solids* **77**, 877 (1985).

[16] Wagner, S., Chu, Shen, D.S., Conde, J.P., Aljishi, S., and Smith, Z.E., "The optoelectronic properties of a-Si,Ge:H(F) alloys," *MRS Symp. Proc.* **118**, 623 (1988).

[17] Aljishi, S., Shu, J., and Ley, L., "The density of states in undoped and doped amorphous silicon-germanium alloys determined through photo yield spectroscopy," *MRS Symp. Proc.* **149**, 125 (1989).

[18] Marshall, J.M., Street, R.A., Thompson, M.J., and Jackson, W.B., "The energy distribution of localized states, and the mobilities of free carriers in a-Si:H, from time of flight and other measurements," *J. Non-Crys.Solids* **97**, 563 (1987).

[19] Wang, N., and Morin, P., *Optoelectronic properties of a-Si,Ge:H alloys* (Princeton University Publications, New Jersey, 1992).

[20] Wang, N., and Morin, P., *Optoelectronic properties of a-Si,Ge:H alloys* (Princeton University Publications, New Jersey, 1993).

[21] Karg, F.H., Hirschauer, B., Kasper, W., and Pierz, K., "Structural and electronic properties of glow discharge deposited a-Ge:H films as a function of the substrate potential," *Solar Energy Materials* **22**, 169 (1991).

[22] Tsutsumi, Y., Okamoto, H., and Hamakawa, Y., "Measurements of gap states in undoped a-SiGe:H alloys by modulated photocurrent spectroscopy," *Phil. Mag. B* **60**, 695 (1989).

[23] Wagner, S., Xu, X., Li, X.R., Shen, D.S., Isomura, M.B., Delahoy, A.E., Arch, J.K., Nicque, J.L., and Fonash, S.J., "Performance and modeling of amorphous silicon solar cells soaked at high light intensity," *Proc. 22 nd IEEE PV Spec.Conf.*, 1307 (1991).

[24] Werner, L., and Tsuo, Y.S., *Hydrogenated amorphous silicon alloy deposition processes* (Marcel Dekker Inc., New York, 1993).

[25] Guha, S., Payson, J.S., Agarwal, S.C., and Ovshinsky, S.R., "Flourinated amorphous Silicon-Germanium alloys deposited from disilane-germane mixture," *J. Non-Crys.Solids* **97**, 1455 (1987).

[26] Paul, W., and Mackenzie, K.D., "Amorphous hydrogenated silicon germanium alloys suitable for photoelectronic applications," *Annual Sub-contract Report, SERI/STR-211*, 3107 (1987).

[27] von Roedern, B., Mahan, A.H., McMohan, T.J., and Madan, A., "An assesment of a-SiGe:H alloys with band gap of 1.5 eV as to their suitability for solar cell applications," *MRS Symp. Proc.* **49**, 167 (1985).

[28] Weller, H.C., Paasche, S.M., Nebel, C.E., Kessler, F., and Bauer, G.H., "Highly photoconductive 1.4-1.5 eV amorphous silicon germanium alloys prepared using glow discharge," *Proc. 19th IEEE PV Spec. Conf.*, 872 (1987).

[29] Rocheleau, R., R.M. Tullman, D.E. Albright, and S.S. Hegedus, "Effects of impurities on film quality and device performance in Si:H deposited by photoassisted CVD," *Proc. 19th IEEE PV Spec. Conf.*, 699 (1987).

[30] Newton, J.L., and Kritikson, K., "Electrical and structural properties of a-Ge:H alloys," *Proc. 21st IEEE PV Spec. Conf.*, 1662 (1990).

[31] Dalal, V., Kaushal, S.K., Xu, J., and Han, K., "A critical review of the growth and properties of a-(Si,Ge):H," *Proc. 21st IEEE PV Spec. Conf.*, 1662 (1990).

[32] Dalal, V., "Comprehensive research on the stability and electronic properties of a-Si:H and a-(Si,Ge):H alloys and devices," *Final Subcontract Report NREL/TP-411*, 7695 (1995).

[33] Brodsky, M.H., Cardona, C., and Cuomo, J., "Various vibrational modes of amorphous silicon," *Phys. Rev. B* **16**, 3556 (1977).

[34] Shanks, H.R., Fang, C.J., Ley, L., Cardona, M., Demond, F.J., and Kablitzer, S., "Infrared spectrum and structure of hydrogenated amorphous silicon," *Phys. Stat. Sol. B* **100**, 43 (1980).

[35] Catherine, Y., and Turban, G., "Infrared absorption of hydrogenated amorphous Si-C and Ge-C films," *Thin Solid Films* **70**, 101 (1980).

[36] Fang, C.J., Gruntz, K.J., Ley, L., Cardona, M., Demond, F.J., Muller, G., and Kalbitzer, S., "The hydrogen content of a-Ge:H and a-Si:H as determined by IR spectroscopy, gas evolution and nuclear reaction technique," *J. Non-Cryst. Solids* **35 & 36**, 255 (1980).

[37] Cardona, M., "Vibrational spectra of hydrogen in Silicon and Germanium," *Phys. Stat. Sol. B* **118**, 463 (1983).

# ACKNOWLEDGMENTS

I would like to take this opportunity to express my sincere gratitude to my major professor, Dr. Vikram Dalal, for his invaluable guidance and support throughout the course of investigation. I would also like to thank Howard Shanks and Dr. Gary Tuttle for serving on my committee. Thanks are also due to Dr. Joe Shinar and Dr. Ruth Shinar for guiding me through the FTIR measurements. The support, help and ever friendly attitude of all the members of Iowa Thin Film group contributed positively towards the successful completion of this project

I would like to thank EPRC for providing the financial support during the past two years of my work at the Microelectronics Research Center.

I am very grateful to Dr.Scott deboer for not only his great friendship but also for giving me the opportunity to get involved in the design and establishment of the new ECR reactor. I gratefully acknowledge Dr. Ralph Knox for his invaluable assistance and suggestions throughout this project. I also take pleasure in acknowledging the technical help from my colleague Keqin Han.

I would also like to thank Mark leonard, Greg Baldwin, Er-Xuan Ping, Russ Bruhn, Bill Liners, Prem Chalal, Francisco Martin, Jun Xu, Flourence, Sandhya Gupta and Swati for their friendship.

Finally, I would like to thank my whole family for their support, patience and love during the course of this study.

# APPENDIX A. ELECTRON MOTION IN A STATIC MAGNETIC FIELD

Free electrons in the plasma generation region spiral around the static magnetic field lines, due to the Lorentz force.

$$\vec{F} = q(\vec{v} \times \vec{B}) \tag{A-1}$$

If we assume that $\vec{B} = B_o \hat{a}_z$, this can be written as shown in Equation A-2.

$$m \frac{d^2x}{d^2t}\hat{a}_x + m \frac{d^2y}{d^2t}\hat{a}_y + m \frac{d^2z}{d^2t}\hat{a}_z = qB_o\left(v_y \hat{a}_x - v_x \hat{a}_y\right) \tag{A-2}$$

By equating components, we get the results shown in Equation A-3.

$$m\frac{d^2x}{d^2t} = qB_o v_y \qquad m\frac{d^2y}{d^2t} = -qB_o v_x \qquad m\frac{d^2z}{d^2t} = 0 \tag{A-3}$$

Now by integrating with respect to t, we get Equation A-4.

$$\frac{dx}{dt} = \frac{qB_o y}{m} + C_1 \qquad \frac{dy}{dt} = -\frac{qB_o x}{m} + C_2 \qquad \frac{dz}{dt} = C_3 \tag{A-4}$$

The result in Equation A-4 can be put back into Equation A-3 to get separated differential equations. For example, the equation for x is

$$\frac{d^2x}{dt^2} + \omega_o^2 x = x_o \omega_o^2 \tag{A-5}$$

where $\omega_o = \frac{qB_o}{m}$ and $_ox = \frac{C_2}{m\,\omega_o}$ . The solution to this equation is

$$x = x_o + R\cos(\omega_o t + \phi) \tag{A-6}$$

where R and F are the constants of integration. By taking the derivative of Equation A-6 we get the x-component of the velocity.

$$v_x = \frac{dx}{dt} = -R\omega_o \sin(\omega_o t + \phi) \tag{A-7}$$

This result can then be substituted back into Equation A-4 in order to get

$$y = y_o - R\sin(\omega_o t + \phi) \tag{A-8}$$

and

$$v_y = \frac{dy}{dt} = -R\omega_o \cos(\omega_o t + \phi) \tag{A-9}$$

where $y_o = \frac{C_1}{m\,\omega_o}$ . Now if we square and add Equations A-6 and A-8 we see that the motion of the electron in the plane perpendicular to the magnetic field is circular with radius R.

$$(x - x_o)^2 + (y - y_o)^2 = R^2 \tag{A-10}$$

From Equations A-7 and A-9 we can solve for the radius.

$$R = \frac{\sqrt{v_x^2 + v_y^2}}{\omega_o} = \sqrt{v_x^2 + v_y^2}\left(\frac{m}{qB_o}\right) \tag{A-11}$$

Since the velocity of the electron in the z-direction (parallel to the magnetic field) is constant, the electron spirals around the z-axis with a frequency of

$$\omega_o = \frac{qB_o}{m} \tag{A-12}$$

and a radius given by Equation A-11 above.

# APPENDIX B. CALIBRATION OF $\alpha_{subgap}$

To calibrate the $\alpha_{subgap}$ obtained from sub-gap photo-conductiviity measurements, we have to be aware of the approximations used in obtaining $\alpha_{subgap}$.

We are assuming that sub-gap photo-conductivity is proportional to the number of absorbed photons. The number of absorbed photons $N_{abs}$, is given by:

$$N_{abs} = \left(1 - e^{-\alpha t}\right) \tag{B-1}$$

where 't' is the thickness of the film.

For regions of photon energy where '$\alpha$' is very small, e.g. 1.0E2 $cm^{-1}$, $N_{abs} = \alpha t$. However, in spectrophotometric measurements, this is not true. Here '$\alpha t$' can be 0.2 or even larger. Hence, we have to make a correction for '$\alpha$' obtained from subgap photoconductivity measurements. The procedure is as follows:

(1) Measure $\alpha$ from spectro-photometric measurements. Typically, $\alpha$ will be in range of 1E3 $cm^{-1}$ and '$\alpha t$' may be 0.2-0.3. Call this $\alpha_R$, for real $\alpha$.

(2) Calculate $\alpha_{pc}$ using the relationship given by

$$\alpha_{pc} = \frac{\left[1 - \exp(-\alpha_R t)\right]}{t} \tag{B-2}$$

This is the photo-conductivity '$\alpha$' which corresponds to the '$\alpha$' being measured in the subgap regime when '$\alpha$' is very small.

(3) Calibrate the subgap curve to actual '$\alpha$' curve by comparing $\alpha_{pc}$, calculated above, with the measured '$\alpha$' from subgap photoconductivity measurements at the

same photon energy. This comparison should be done at several photon energies to reduce calibration errors, and should give the correct multiplier factor for the subgap photoconductivity curve. Note that the correction factors will be different at different photon energies (i.e., the correction for 1.7eV photons may be different from 1.75eV because of the non-small $\alpha t$ at 1.75eV). However, only one calibration factor for the low energy photoconductivity curve should result if measurements are made carefully, and the above procedure applied correctly.